OPTIMIZATION OF PROPERTIES OF ZIRCONIA-MULLITE CERAMICS

N.S. Carr

A dissertation submitted to the Faculty of Engineering, University of the Witwatersrand, Johannesburg, for the degree of Master of Science in Engineering.

Johannesburg, 1989

This dissertation is dedicated to my family.

ACKNOWLEDGEMENTS

I wish to thank the following people and organizations who have been involved in this project.

Dr A.W. Paterson for his guidance on the structure of this dissertation, his enthusiasm, and particularly the time he made available for discussion during the final stages.

Dr R.B. Tait for smoothing the way and his pragmatic advice.

Mrs D.A. Jones for her infectious enthusiasm and exceptional assistance in the laboratory.

Mrs Adele Forman for the typing and cheerfully accepting the endless corrections.

The Division of Materials Science and Technology (DMST), CSIR for financial and management support, and in particular to all my colleagues for their help.

Multotec Manufacturing (Pty) Ltd for their financial support and for allowing this dissertation to be published.

ABSTRACT

A SrO-doped partially reacted zircon-alumina-zirconia-mullite has been developed which is competitive with commercial 90% alumina in abrasive wear resistant applications. The material properties were optimized using statistical, experimental design, multi-factor analysis and hill climbing techniques. SrO was selected after a preliminary study of a number of dopants including CaO, SrO, BaO, ZnO and some combinations of these. A particular investigation was also carried out on the effect of BaO on zircon using conventional, XRD and SEM techniques. A comprehesive literature review of zirconia-mullite processing and properties forms the basis of the study.

DECLARATION

I declare that this dissertation is my own, unaided work. It is being submitted for the degree of Master of Science in Engineering in the University of the Witwatersrand, Johannesburg. It has not been submitted before for any degree or examination in any other University.

____

(Signature of candidate)

________ day of ________ 19__

CONTENTS

CONTENTS (Cont.)

Page

CONTENTS (Cont.)

CONTENTS (APPENDIX)

SECTION 1: LITERATURE SURVEY

1. INTRODUCTION AND HISTORICAL BACKGROUND

1.1 *INTRODUCTION*

The incorporation of ZrO_2 as a dispersed second phase in a ceramic matrix is known to result in improved mechanical properties, owing to the operation of a number of toughening and strengthening mechanisms [1-4]. Most of the research in this field has concentrated, over the past decade, on zirconia-alumina. These materials are now being developed commercially as engineering ceramics and have already found use as cutting tools in favour of alumina [5,6]. More recently, increasing interest has been shown in other composite ceramics containing zirconia, particularly in zirconia-mullite [7-10]. This interest is reflected by the growing publication rate illustrated from a recent literature search (Fig. 1).

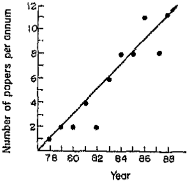

FIGURE 1: Number of publications per annum on zirconia-mullite

One of the disadvantages associated with zirconia-toughened composites is the high cost of ZrO_2 purified from zircon ($ZrSiO_4$) by chemical or thermal processing. Zirconia-mullite, however, can be produced *in situ* from zircon by virtue of the reaction;

$$\underset{\text{zircon}}{2ZrSiO_4} + \underset{\text{alumina}}{3Al_2O_3} \xrightarrow{\sim 1\ 550\ C} \underset{\text{zirconia}}{2ZrO_2} + \underset{\text{mullite}}{3Al_2O_3.2SiO_2} \qquad (1)$$

This processing route has been successfully used to produce ceramics with good mechanical properties, compared to pure mullite as shown in Table 1. The literature sources of the data are shown in square brackets.

TABLE 1: Comparison of mullite and zirconia-mullite properties

Ceramic Material	Fracture Toughness K_{Ic} (MPa.m$^{1/2}$)		Fracture Stress σ_f (MPa)	
	Single edge notch beam	Vickers indentation	3-point bend	4-point bend
Mullite	2,2 [11]	2,2 [12]	215 [12]	269 [13]
Zirconia-mullite	4,5 [14]	3,5 [15]	330 [16]	400 [14]

More importantly, the mechanical properties of zirconia-mullite are comparable to those for alumina, typical strength and toughness data for which are 350 MPa and 4,0 MPa.m$^{1/2}$ respectively [17]. In addition, wear by particle impact erosion shows good cost competitiveness between zirconia-mullite and alumina [15]. This has important commercial implications. The mining and power industries use considerable volumes of debased alumina tiles for protecting a variety of steel components against abrasive wear in ore, fuel and ash handling situations. Plate 1 illustrates a typical application.

The purpose of this present study was to develop a reaction-sintered zircon-alumina body that would be cost competitive with commercial 90% alumina tiles in wear resistant applications. Extensive use was made of statistical experimental design, analysis and optimization techniques. The dissertation has been divided into two sections for convenience. The first discusses the literature of zirconia-mullite pertaining to conventional processing. The second describes the experimental design and methodology used, results, discussion and conclusions.

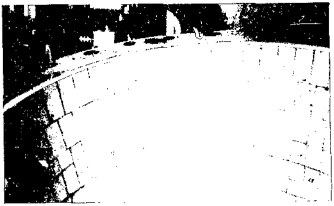

PLATE 1: Ceramic tile lined mild steel bend. Courtesy of Multotec Manufacturing (Pty) Ltd.

The use of the terms zircon-alumina and zirconia-mullite requires some flexibility. In the literature they appear to be used interchangeably with zirconia-mullite tending to be favoured as the generic name. In this dissertation a distinction between the two has been attempted on the basis of the phases existing in the final sintered body. Zirconia-mullite is used to refer to a fully reacted stoichiometric ceramic. Zircon-alumina on the other hand is used to describe ceramics formed by partial reaction or which are non-stoichiometric with respect to final zirconia-mullite formation. In this latter case the term zirconia-mullite may be misleading.

1.2 *HISTORICAL BACKGROUND*

In order to put zirconia-mullite research into perspective an overview of its historical development has been made. This is represented diagrammatically in Fig. 2. As a generalization, current research can be said to have developed from two research areas, namely a mechanistic processing approach and a material properties approach. Mechanistic processing research tends to place emphasis on phase equilibria studies and thermal properties of materials whereas material properties research places emphasis on mechanical properties in relation to microstructure. Owing to interest in high temperature resistant materials on the one hand and low cost toughened ceramics on the other, both areas of research have merged with their respective traits.

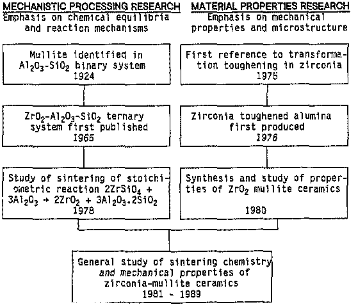

FIGURE 2: Historical development of zirconia-mullite research

1.2.1 *Mechanistic Processing Research*

Historically a key event in the development of zirconia-toughened mullite can probably be said to date from the identification of mullite by Bowen and Greig in 1924 in a study of the alumina-silica binary system [18]. They determined its composition as $3Al_2O_3.2SiO_2$. There have since been reports of another form of mullite with the formula $2Al_2O_3.SiO_2$ [13,18]. These formulae represent an alumina compositional range of 71,8 - 77,3 wt.%. The more usual form, $3Al_2O_3.2SiO_2$, is the form which will referred to as mullite in the text unless otherwise specified. This material has been shown to possess excellent properties both as a refractory and as an engineering ceramic. It exhibits good chemical and thermal stability, high refractoriness, low creep rate, low thermal expansion and thermal conductivity, medium strength and toughness and, finally, useful dielectric properties. Some of these properties are compared against high purity alumina in Table 2 [17].

TABLE 2: Comparison of physical properties of alumina and mullite

Property		Value		Units
		Alumina	Mullite	
Thermal expansion coefficient,	α	8,1	5,0	(25-800 C) (10^{-6}/C)
Dielectric constant	ε	9,5	6,6	(25 C, 1 MHz)
Bend strength	σ_f	350	270	(MPa)
Fracture toughness	K_{Ic}	4,0	2,6	(MPa.$m^{½}$)
Vickers hardness	H_v	18,0	11,0	(GPa)
Young's modulus	E	400	220	(GPa)
Poisson's ratio	ν	0,25	0,27	

The preparation of mullite in the refractories industry is usually by thermal decomposition of a mineral such as kaolinite in an electric arc furnace. Impurities present and non-stoichiometry cause the formation of liquid phases which result in the growth of columnar needles and the formation of other alumino-silicate phases as well as considerable porosity. Once crystallized, mullite is particularly resistant to morphological change owing to low ionic diffusivities in its structure. For this reason pure mullite is extremely difficult to sinter.

In addition to alumino-silicates, zircon is also widely used in refractory and foundry applications, both in its own right and as a precursor to zirconia after decomposition. This decomposition occurs in the range 1 500 - 1 650 C to form zirconia and an armorphous silica phase according to eq. 2.

$$ZrSiO_4 \xrightarrow{1\ 500\ -\ 1\ 650\ C} ZrO_2 + SiO_2 \qquad (2)$$

Owing to the reversible nature of the reaction zircon does not decompose fully on its own. The wide decomposition temperature range is a reflection of the effect of impurities on the system which in turn affect the zirconia phases present on cooling. This difficulty in clearly defining the zircon system probably accounts for the shortage of phase diagrams on zirconia-silica-metal oxide systems until relatively recently.

In order to assist the dissociation (eq. (2)) one of the two products, zirconia or silica, has to be removed from the system. This is conveniently done by the thermodynamically favourable reaction,

$$3Al_2O_3 + 2SiO_2 \xrightarrow{\sim 1\ 200\ C} \underset{\text{mullite}}{3Al_2O_3.2SiO_2} \qquad (3)$$

Alumina-zirconia-silica ceramics are used in a wide variety of applications as feeder parts, kiln furniture, crucibles and furnace linings. The ternary phase diagram describing the system was first published in 1965 (Fig. 3). Materials based on this system are usually made by fusion casting or pressureless reaction sintering of zircon and alumina. *Interest in the reaction and* densification kinetics of the stoichiometric reaction described in eq. (1) necessitated the use of purer reactants and more stringent

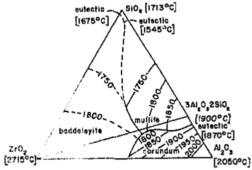

FIGURE 3: Phase diagram of the system ZrO_2-Al_2O_3-SiO_2 (after Budnikov and Litvakovskii) - pg. 363 ref [18]

preparative techniques than is generally required in the refractories industry. The first study of this nature was reported by Di Rupo, Carruthers and Brook in 1978 [7] coinciding with the interest being shown in zirconia toughened engineering ceramics.

1.2.2 *Mechanical Properties Research*

Mechanical properties ceramics research places emphasis on the processing of a material by control of its final microstructure so as to attain desired mechanical properties. This requires special attention to raw material purity and physical morphology (e.g. particle size distribution), and carefully controlled processing routes often involving pressure sintering.

The sintering of high purity dense mullite has proved to be difficult. It is critically dependent on stoichiometry [11] and requires sub-micron powders [11,13]. Sintering for several hours at 1 600 C has been shown to produce ceramics of ~97% theoretical density and moderate strength (~200 MPa : biaxial flexure on 30 mm diameter discs) [11]. Fully dense (3,19 g/cm^3) mullite has been produced from amorphous alumino-silicates produced by hydrolysis of the stoichiometrically mixed alkoxides [13]. This material was hot-pressed under vacuum at 6,8 MPa and 1 500 C for 30 minutes and found to have a strength of 269 MPa in 4-point bending. Hot pressing is necessary to attain theoretical density owing to the great difficulty in sintering pure crystallized mullite. A mullite has also been produced by Ismail and co-workers [19] with a reported flexural strength of 385 MPa. The mullite was synthesized by calcining a boehmite-silica gel which was cold isostatically pressed at 200 MPa and sintered to 98% density at 1 650 C for 3 hours.

The studies by Di Rupo and co-workers [7-10] of reactions taking place in the Al_2O_3-ZrO_2-SiO_2 system including the stoichiometric zircon-alumina reaction, was approximately concurrent with the discovery of toughening owing to the martensitic tetragonal to monoclinic (t→m) transformation in zirconia [20]. Using this concept, Claussen and Jahn [14] demonstrated the potential toughening effects by incorporating zirconia in a mullite matrix. This was achieved by manipulating the densification and reaction steps of stoichiometric zircon-alumina mixes. A two-stage sintering sequence (Fig. 4) was used to sinter an attrition milled stoichiometric mix at 1 400 C for 2 hours initially, followed by 1 hour at 1 600 C. This produced a dense material (3,76 g/cm^3, >98%) with good strength (400 MPa) and toughness (4,5 MPa.m^{½}). These figures are compared with other data in Table 1.

Since the work by Di Rupo et al. and Claussen and Jahn, interest in the zircon-alumina system has been steadily increasing. However, progress in understanding and controlling the processing and properties has been relatively slow when compared with, for example, the zirconia-alumina system. This is undoubtedly due to the complexity of the reaction mechanisms involving zircon, alumina, mullite, zirconia, silica, various impurities or dopants and pores. The toughening and strengthening mechanisms in the zirconia-alumina system are, in addition, not directly transferable to the interpretation of zirconia-mullite. Currently there is considerable research activity which has, as yet, to reach a unified basis for interpretation.

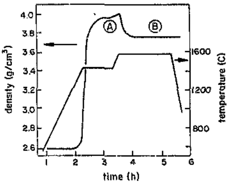

FIGURE 4: Diagramatic representation of 2 stage reaction sintering schedule of Claussen and Jahn [14]. At (A) only zircon and alumina were detected. At (B) the reaction to zirconia and mullite is complete

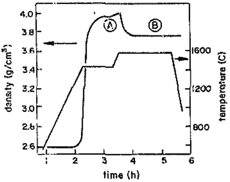

FIGURE 4: Diagramatic representation of 2 stage reaction sintering schedule of Claussen and Jahn [14]. At (A) only zircon and alumina were detected. At (B) the reaction to zirconia and mullite is complete

2. REACTION SINTERING THEORY

Reaction sintering in the Al_2O_3-[illegible]-SiO_2 system can be divided into two areas for consideration, namely chemical and physical. These will be considered separately in this section.

2.1 *LIQUID PHASE SINTERING*

A major physical disadvantage in the processing of dense zirconia-mullite is the need for high temperatures and pressures. This has serious cost implications in commercial production. The use of suitable dopants that form liquid phases during sintering is one way of overcoming this difficulty. Sections 2.2.3 and 2.2.4 on the quaternary systems will outline the potential of liquid phase sintering from a largely chemical viewpoint. In general the zirconia-mullite literature concentrates on processing in relation to microstructure and properties and does not concern itself with the actual mechanism of sintering. A majority of ceramics are fabricated with liquid phases present during sintering as has been the case for centuries with pottery and bricks among others. Liquid phase sintering generally provides sufficient internal force through capillary action to achieve the equivalent of very large external pressures, thereby obviating the need for expensive processing technology.

There are, however, many practical disadvantages. Among these are liquid phase exudation, compact slumping, excessive grain growth and large pore formation. From a theoretical point of view the difficulties of predicting behaviour are enormous. During sintering there are three physical phases present namely solid, liquid and vapour. In a magnesia-doped zircon-alumina body reacting to form spinel, mullite, tetragonal and monoclinic zirconia with the transient appearance of saphirine there are at least eight chemical phases and also transient and permanent liquid phases present at one time or another. This results in multiple solubility, viscosity and diffusivity effects interacting with the various interfacial energies, ionic mobilities and general thermodynamic effects. Controlling liquid phase sintering is therefore necessarily an empirical affair, usually involving the manipulation of heating rates, soak time and temperatures together with other controllable parameters such as dopant concentration and particle size of raw materials.

2.2 *CHEMICAL ASPECTS OF REACTION SINTERING*

There are two main processing routes to zirconia-mullite ceramics. The first and most important commercially is by reaction sintering zircon and alumina as represented by equation (1). The second which is more of research interest is by reaction sintering a pre-mullite powder with zirconia as represented in equation (4)

$$3Al_2O_3 + 2SiO_2 + xZrO_2 \longrightarrow 3Al_2O_3.2SiO_2 + xZrO_2 \qquad (4)$$

The transformation of zircon and alumina to zirconia and mullite can be represented by the single scheme shown in Fig. 5, showing clearly the two distinct stages of the reaction namely zircon decomposition and mullitization. Figure 5 can also be represented in thermodynamic terms as illustrated in Fig. 6 [10].

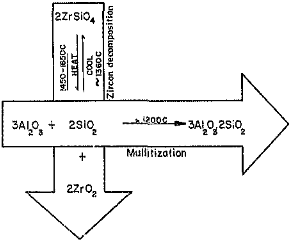

FIGURE 5: Schematic representation of zircon-alumina reaction to form zirconia-mullite

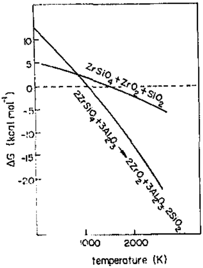

FIGURE 6: Gibbs function (ΔG) versus temperature for the zircon-alumina → zirconia-mullite reaction after Di Rupo and Anseau [18]

These two stages will be considered in turn followed by a brief description of two quaternary systems consisting of Al_2O_3-ZrO_2-SiO_2 and CaO and MgO respectively.

2.2.1 *Dissociation of zircon*

In the reaction represented in Figs 5 and 6 it is important to control the kinetics of the dissociation of zircon or modify the thermodynamics as this has a direct effect on the formation of mullite and hence the microstructure and properties of the final material. Pena and De Aza [21] reviewed the thermal stability of zircon as reported by a number of authors since 1920. They found considerable disagreement with reports of congruent melting at 2 430 C and 2 550 C, incongruent melting at 1 775 C, and dissociation from 1 400 - 2 000 C. They attributed this disagreement to incorrect analysis of experimental results, poor analytical techniques and the use of zircon with large differences in the nature and proportion of impurities. A typical analysis for zircon mined at Richard's Bay in Natal (RSA) is given in Table 3, showing a total impurity content of ~0.8%.

TABLE 3

Material	Zircon
Supplier	Ferro Industrial Products* Brakpan, South Africa
Type	F.Z.O. S/F
Average particle size (µm)**	0,9
% ZrO_2	65,9
% SiO_2***	32,0
% Al_2O_3	0,12
% TiO_2	0,1
% CaO	0,09
% Fe_2O_3	0,08
% MgO	0,02
% Na_2O	-

* Mined by Richard's Bay Minerals, Richard's Bay, Natal, South Africa.
** Sedigraph 5000
*** Approximately 0,4% as free SiO_2.

The effect of these impurities can be elucidated with reference to Figs 7-9 [21]. Figure 7 represents the binary system of ZrO_2-SiO_2 showing the decomposition of zircon occurring at 1 676 C. Zircon sand, however, has significant impurities of SiO_2, Al_2O_3 and TiO_2. Owing to their low concentration in zircon these will exist in the sub-system zirconia-titanate, zircon, mullite and silica of the quaternary system ZrO_2-Al_2O_3-SiO_2-TiO_2 as shown in Fig. 8. The first formation of a liquid phase will be at the 1 450 C invariant point in the sub-system represented by 's' in Fig. 9. This is 226 C lower than that for the binary system in Fig. 7.

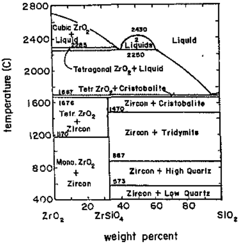

FIGURE 7: ZrO_2-SiO_2 system [21]

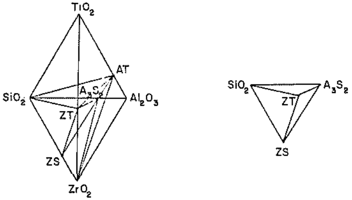

FIGURE 8: Solid state relationship in the ZrO_2-Al_2O_3-TiO_2 system, (excluding solid solutions) [21]

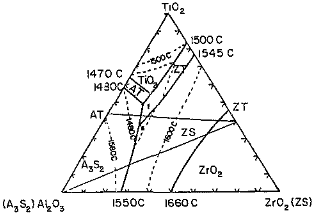

FIGURE 9: Projection through SiO_2 of the ZrO_2-Al_2O_3-SiO_2-TiO_2 system showing phase boundaries and isotherms [21]

The situation represented above is necessarily a simpler case than that likely to occur in practice as it omits the presence of solid solutions and other contaminants such as Fe_2O_3 that may be present. However, it serves to illustrate the effect of low impurity concentrations in forming small quantities of liquid phase that could have an enhancing effect on rates of reaction and densification. The presence of liquid phases containing silica and titania has been demonstrated by Pena *et al.* [22] in sintered zircon as well as reaction zones between rutile and zircon. While these inclusions usually occur between grains, glassy phases have also been *detected within zircon grains. Pena and de Aza argued* that although the presence of impurities lowers the dissociation temperature of zircon this is insignificant compared to the large lowering of temperature at which liquid phases first appear [21]. Assuming the validity of this argument the presence of impurities dominates the kinetics rather than thermodynamics of the system.

2.2.2 *Reaction of Al_2O_3 and SiO_2 (mullitization)*

The mullite system can be better appreciated by considering the development of the binary phase diagram of SiO_2 and Al_2O_3. Despite being the subject of considerable research over the years the literature remains contradictory. This may be due to the sluggish kinetics often present in these systems, resulting in differences of interpretation. Metastable phases and solid solutions, both highly susceptible to processing conditions, can occur which complicates the analysis of such a system.

Bowen and Greig [23] first constructed a binary Al_2O_3-SiO_2 phase diagram in 1924 (Fig. 10). This diagram shows the presence of pure mullite which melts incongruently at 1 830 C and having a fixed composition, $3Al_2O_3.2SiO_2$ (71,8 wt.% Al_2O_3). Subsequently, however, there have been conflicting reports, in particular the identification of mullites of composition, $2Al_2O_3.SiO_2$ (77,4% Al_2O_3) and congruent melting of mullite. Aramaki and Roy [24] revised the phase diagram showing a stable mullite solid solution in the range 71,8 - 74,3 wt.% (Fig. 11). They also demonstrated that mullites can be prepared from the 3/2 ratio up to 2/1, indicating the possible presence of mullite with an alumina content up to 77,4%. This latter material was prepared by arc-melting pure kaolinite and hydrated alumina. This work permitted an explanation of the observed congruent melting, showing a melting point of 1 850 C, but did not explain the incongruent melting observed earlier (Fig. 10).

It was Aksay and Pask [25] who explained both melting modes using a diffusion couple experimental technique developed by Davis and Pask [26]. This technique has proved effective for obtaining stable and metastable phase equilibrium data. Incorporating their results with those of other workers they proposed the phase diagram illustrated in Fig. 12.

The diagram shows the presence of a stable mullite solid solution, a metastable silica-ordered mullite solid solution and a metastable silica-disordered mullite solid solution. The stable

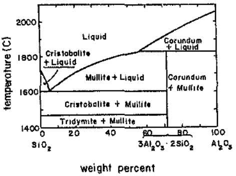

FIGURE 10: The Al_2O_3-SiO_2 system after Bowen and Greig [23]

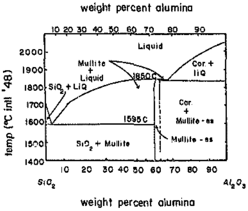

FIGURE 11: The Al_2O_3-SiO_2 system according to Aramaki and Roy [24]

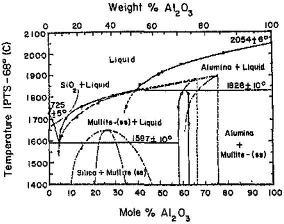

FIGURE 12: The Al_2O_3-SiO_2 system according to Aksay and Pask [25]

mullite has a solid solution range from 71,6 - 74,0 wt.% Al_2O_3 at 1 813 C, melts incongruently at 1 830 C in agreement with Fig. 10, however, can melt congruently if superheated.

The silica-ordered mullite has a solid solution range up to ~77 wt.% Al_2O_3 and melts congruently at ~1 880 C while the silica-disordered mullite has a range extending to ~83 wt.% Al_2O_3 and melts at 1 900 C. Aksay and Pask [25] concluded that metastable phase equilibria result from various difficulties associated with nucleation of phases. In general mullite formed at temperature by a solid state reaction is ordered and of the $3Al_2O_3.2SiO_2$ type while mullite formed from a liquid phase is disordered and of the $2Al_2O_3.SiO_2$ type.

The presence of dopants and impurities further complicates the Al_2O_3-SiO_2 binary system, however, despite a large number of investigations (reviewed by Rodrigo and Boch [11]) definite conclusions cannot be drawn. This is due to contradictory information, a result of lack of precise details and the use of natural raw materials which may have introduced impurity effects. Difficulties with experimental techniques may also cause problems. Dopants or impurities often exist in solid solutions, analysis of which requires sophisticated techniques. Solid solutions of ZrO_2 in mullite have been studied [27,28] and up to 35% ZrO_2 has been reported.

Solid solutions have also been reported for other oxides namely Fe_2O_3, Cr_2O_3 and TiO_2 with solubilities of respectively 10-12% above 1 300 C, 8-10 wt.% above 1 600 C and 2-4% above 1 300 C [11]. The solid solutions cause an increase in unit cell volume. It appears that the presence of Fe_2O_3, TiO_2, CaO and ZrO_2 facilitate mullitization although there is contradictory evidence on the effect of Fe_2O_3 [11].

2.2.3 *The Al_2O_3-ZrO_2-SiO_2-CaO system*

From the foregoing discussion it is clear that in conventional ceramics processing any discussion of the Al_2O_3-ZrO_2-SiO_2 system has to take cognizance of the effects of impurities. The possible impact of these effects can be gained by considering the work done on four phase systems by Pena *et al.* [29-31]. These studies concerned the quaternary systems ZrO_2-Al_2O_3-SiO_2-XO where XO represents CaO, MgO and TiO_2 respectively. The TiO_2 system has been discussed above in Section 2.2.1. The CaO and MgO systems will now be discussed briefly.

In the Al_2O_3-ZrO_2-SiO_2-XO system, Pena *et al.* specifically studied the reaction;

$$(2+2X)\ \underset{\text{zircon}}{ZrSiO_4}+3Al_2O_3+X(Al_2O_3+CaO) \rightarrow$$

$$(2+2X)\ ZrO_2+\underset{\text{mullite}}{3Al_2O_3.2SiO_2}+X\underset{\text{anorthite}}{CaAl_2Si_2O_8} \qquad (5)$$

where X was equal 0, 0,3 and 1 [29]. The relevant phase diagram is shown in Fig. 13. The progress of reaction was followed by dilatometry (Fig. 14) and quantitative XRD (Fig. 15). The XRD analysis of the different phases was in terms of the relationships,

$$\alpha = \frac{C_Z}{C_Z + C_{ZS}} \qquad \text{and} \qquad \beta = \frac{C_m}{C_m + C_A}$$

where C_Z, C_{ZS}, C_m and C_A are the concentrations of zirconia, zircon, mullite and alumina respectively.

The presence of CaO had a significant effect on both densification and reaction. The shrinkage behaviour for χ=0 and χ=1 (Fig. 14) are quite different. Where no CaO was present shrinkage was smooth with respect to temperature. However, with χ=1 two stages were observed. Initially, (1 200-1 400 C) shrinkage was reduced relative to the undoped material while above 1 400 C the contraction increased significantly beyond that for the undoped material.

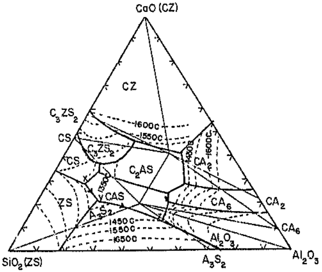

FIGURE 13: Projection through the ZrO_2-corner showing secondary phases crystallizing during freezing from ZrO_2-Al_2O_3-SiO_2-CaO mixtures containing 60 wt.% ZrO_2 [29]

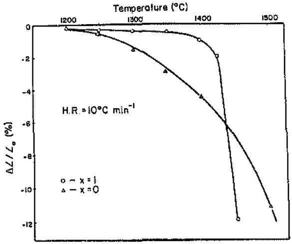

FIGURE 14: Shrinkage of $X=0$ and $X=1$ samples as a function of temperature [29]

The evolution of both mullite and zirconia was observed at 1 425 C with respect to time (Fig. 15). With $X=0$ the decomposition of zircon and appearance of mullite occurred simultaneously. Increasing additions of CaO increased the rate of decomposition of zircon and formation of mullite, however, the presence of CaO resulted in a delay before mullitization began.

These effects on both shrinkage and reaction can be explained by the formation of anorthite at ~1 200 C when CaO is present. Recently Rincon *et al.* [32] studied the reaction with $X=1$ using XRD, electron microscopy and microanalysis. They summarized the reaction sequence by the scheme shown in Fig. 16. The reaction starts with the formation of anorthite and decomposition of zircon. The local co-existence of anorthite, zircon and zirconia produces a transient liquid phase corresponding to the lowest invariant point of the ZrO_2-Al_2O_3-SiO_2-CaO system at 1 200 C (Point x in Fig. 13). This non-equilibrium situation proceeds towards the final peritectic equilibrium point at 1 440 C in the zirconia-mullite-anorthite system (X→Y→Z in Fig. 13). At higher

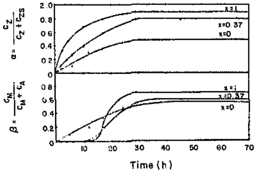

FIGURE 15: Evolution of α and β for compositions X=0, 0,37 and 1 as a function of time, at 1 425 C [29]

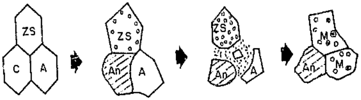

FIGURE 16: Scheme of the reaction sintering of ZrO_2-Al_2O_3-SiO_2-CaO after Rincon *et al.* [32]. Z = ZrO_2, C = CaO, A = Al_2O_3, An = $CaAl_2Si_2O_8$, M = $3Al_2O_3.2SiO_2$, ZS = $ZrSiO_4$

temperatures, anorthite disappears and a permanent liquid phase is present together with alumina, mullite and zirconia. It was also shown that as the mullite grains grow they trap some ZrO_2 particles, and alumina grains which are prevented from reacting.

The microstructure of the CaO doped material showed mullite grains with an elongated rectangular prism morphology. The dimensions ranged from 5-10 µm in length and 1-2 µm wide. Two types of zirconia were observed; one had a particle size of <1 µm, was spherical and intragranular while the other was intergranular, equiaxed and had a particle size of 1-2 µm [29].

2.2.4 *The Al_2O_3-ZrO_2-SiO_2-MgO system*

Investigating the Al_2O_3-ZrO_2-SiO_2-MgO system Miranzo and co-workers [30] studied the reaction,

$$\underset{\text{zircon}}{2ZrSiO_4}+3Al_2O_3+X(Al_2O_3+MgO) \rightarrow 2ZrO_2+\underset{\text{mullite}}{3Al_2O_3.2SiO_2}+X\underset{\text{spinel}}{Al_2MgO_4} \tag{6}$$

As with the previous study the compositions investigated were those with X=0, 0.3 and 1. The relevant phase diagram is shown in Fig. 17. The reaction sintering was followed by XRD and dilatometry. XRD showed the formation of spinel (Al_2MgO_4) below 1 350 C; the presence of spinel, zirconia and saphirine ($Al_{10}Mg_4Si_2O_{33}$) between 1 350 C and 1 425 C, and finally the formation of ZrO_2, spinel and mullite between 1 425 C and 1 450 C with the disappearance of saphirine. The presence of a liquid phase accelerated the shrinkage (Fig. 18), however, there was no initial delay in shrinkage or mullitization (Fig. 19) as reported for the CaO doped system.

Zircon decomposition and mullitization occurred simultaneously, both increasing with increased MgO content. Microstructures of the MgO doped material showed considerable porosity. A more recent paper by Miranzo *et al.* [33], however, shows much more compact microstructures obtained with the same system.

2.3 *PHYSICAL ASPECTS OF REACTION SINTERING*

Whereas the chemical aspects of reaction-sintering can largely be described in thermodynamic terms, the physical aspects are more

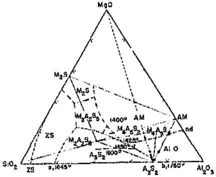

FIGURE 17: Tentative projection of the primary volume of crystallization of ZrO_2 on the opposite face (Al_2O_3-MgO-SiO_2) of the tetrahedron Al_2O_3-MgO-SiO_2-ZrO_2, showing phase boundaries isotherms and solid state compatibilities [30]

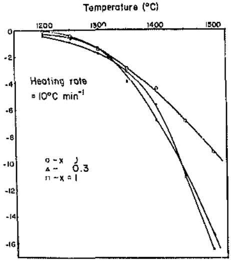

FIGURE 18: Sample shrinkage against temperature for three compositions x=0, 0,3 and 1 [30]

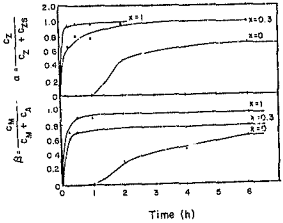

FIGURE 19: Evolution of reaction for x=0, 0.3 and 1, plotted against time at 1 450 C [30]

conveniently approached from a kinetic point of view. Reaction-sintering essentially involves two interacting phenomena, namely densification and reaction. In the zirconia-mullite system both occur by ionic diffusion of the initial species.

The diffusion occurs by ionic movement down stress gradients created by applied pressure; chemical potential gradients dictated by thermodynamic equilibria; and by the existence of surfaces of differing curvature. A major problem of analysing densification kinetics has been that of separating the contributions from different processes such as particle rearrangement, plastic flow, lattice diffusion, and grain boundary or second-phase diffusion. A procedure has been developed [7] for identifying successive stages in densification and is based upon the link that occurs between densification rate and reaction rate for a system in which the same diffusing ion is responsible for both processes.

For such a situation the relative rate of densification and relative rate of reaction are described by the equation,

$$\frac{1}{V_t} \cdot \frac{d\rho}{dt} = - \frac{G}{5} \cdot \frac{1}{V_t} \frac{dV}{dt} \qquad (7)$$

where ρ and V represent the density of the green body and the concentration of one of the original constituents respectively. The t subscript indicates the instantaneous value at time t, S is the probability *that the diffusing atom takes part* in the reaction, and G is a geometrical factor which depends on the model used. Based on the grain boundary diffusion model proposed by Coble (Fig. 20) for deformation by grain - boundary diffusion [34,35], G has been calculated to have a value of $^{2}/_{3}$ [35].

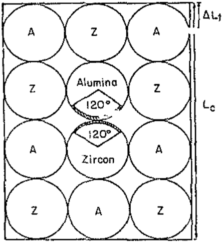

FIGURE 20: Diagrammatic representation of the proposed grain boundary diffusion model of Coble. The reacting grains are assumed to be spheres, and material diffuses through boundary layers to the grain surfaces adjacent to pores. After Anseau *et al.* [36]

Di Rupo *et al.* [7] proposed that the relative rates *of densification* and reaction for hot-pressed reaction-sintered zirconia-mullite should follow that described by Fig. 21. The rates can be seen to proceed in three distinguishable stages. Initially (A), densification rate greatly exceeds reaction rate. This stage is characterized by particle rearrangement, Secondly (B) it is assumed that both *densification and reaction occur by grain boundary* diffusion and the slope of the curve is representative of geometrical and statistical constraints. Finally (C), full densification has occurred and final reaction by diffusion processes occur. The nature of the plot described (Fig. 21) changes with *differing applied pressures and temperatures* and these effects will be discussed in the subsequent two sections.

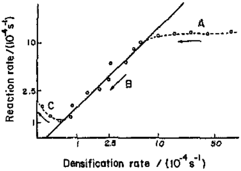

FIGURE 21: Plot of reaction rate and densification rate for hot-pressed zircon/alumina, after Di Rupo *et al.* [7]

2.3.1 *Hot-press reaction sintering*

Di Rupo *et al.* [8] studied hot-press reaction sintering of zircon-alumina based on *Coble's creep equation* [35],

$$\frac{d\rho}{dt} = \frac{47,5\ D_b\ w\ \Omega}{L^3 kT} P_a \tag{8}$$

where D_b is the controlling diffusion coefficient in the boundary phase, w is the width *of the boundary phase, L is the grain size,* Ω the volume of zircon and alumina transported by one atom of the rate-controlling species and P_a the applied pressure.

The densification rate was shown to be linearly dependent on applied pressure in agreement with Coble. Of particular interest was the effect of dopants on the densification rate. Figure 22 shows the effect of Na_2O dopant addition on the densification rate at the temperature and pressure shown. *This was interpreted as* increasing the boundary width w in equation (8), as explained in equation (9),

$$w = w_o + k\,[Na_2O] \qquad (9)$$

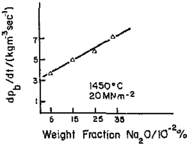

FIGURE 22: Relationship of densification rate of zircon-alumina on the variation of Na_2O content [8]

where w_o is boundary thickness in an undoped sample, k is a constant and $[Na_2O]$ is the concentration of Na_2O. From the intercept it was deduced that in the limit of the model there was a boundary phase layer equivalent to ~0,25% Na_2O. This was in close agreement to the analysis of impurities in the zircon and alumina given as % MO and M_2O.

The densification and reaction rates were measured on an undoped stoichiometric mix at constant temperature with varying applied pressure and at constant pressure with varying temperature. The results are shown in Figs 23 and 24 respectively and in both cases show that the pattern follows that outlined in Fig. 21.

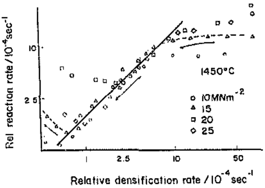

FIGURE 23: *Relationship between densification and reaction rates* for zircon-alumina reacted under different pressures as reported by Di Rupo *et al.* [8]

2.3.2 ***Pressureless reaction sintering***

The relative densification and reaction rates were similarly studied for pressureless reaction sintering at different temperatures as shown in Fig. 25 [9].

The definition between the three stages is much less clear than for the hot-pressed system, particularly at lower temperatures.

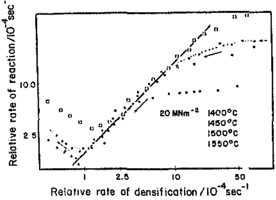

FIGURE 24: Comparison of reaction rate and densification rate for hot-pressed material [9]

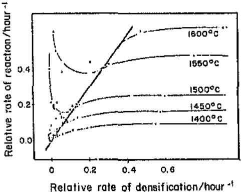

FIGURE 25: Comparison of reaction and densification rates for pressureless reaction-sintered zircon-alumina, after Di Rupo *et al.* [9]

These differences are clearly shown by comparing the densification profiles of hot-pressed and pressureless sintering illustrated in Figs 26 and 27 respectively. In pressureless sintering the lower temperatures show a clear densification profile. This anomaly is due to the reactants having a higher density (~4,3 g/m^3) than the products (~3,8 g/cm^3) and densifying faster than the reaction. This means that the model based on the same ion involved in densification being involved in reaction does not hold true under all conditions. This variability was used to advantage by Claussen and Jahn [14] as has already been described in Fig. 4. The densities achieved for zirconia-mullite by simple profile sintering without pressure are low, giving values of about 96% of the theoretical density. Densifying the reactants prior to reaction attains greater than 98% of theoretical density.

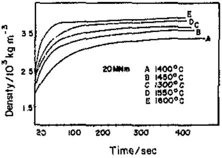

FIGURE 26: Densification data during hot-pressing of zircon-alumina at constant pressure and varying temperature [9]

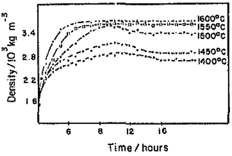

FIGURE 27: Densification data during pressureless sintering of zircon-alumina at varying temperatures [9]

2.4 *SUMMARY*

Reaction-sintering pure zirconia-mullite is a complex process requiring high temperatures and pressures which presents certain limitations to its wide-spread commercial use. Hot-press reaction-sintering at suitable pressures and temperatures can result in a *steady-state densification/reaction* relationship. At lower sintering temperatures and in the absence of pressure, however, there is a tendency for reactants to densify prior to reaction. This phenomenon has been exploited to achieve high density ceramics in the absence of applied pressure.

The addition of suitable dopants has the facility of lowering the densification and reaction temperatures which is commercially *attractive. The doped systems are, however, complex* and detailed knowledge of the interaction of phase chemistry with the physical processes of sintering is essential to producing good quality ceramic bodies.

3. MECHANICAL PROPERTIES AND PROCESSING

Zirconia-mullite research has developed rapidly since its inception and research interests now cover a wide range. A survey of recent publications (post 1985) covers a range of topics including slip casting [37]; processing from plasma sprayed zircon [38], dissociated zircon [39], amorphous zircon and alumina [40]; and development of SiC whisker reinforced bodies [41]. Investigations of microstructure and properties are using more sophisticated techniques including TEM [42]; acoustic emmission [43] and cathodoluminescense [44]. These studies are not directly addressed here as the focus of the present work is on strengthening and toughening mechanisms. This section therefore describes the salient factors affecting toughening and strengthening mechanisms in ceramics in general with reference to zirconia-mullite studies where available. There then follows a general description of processing effects on microstructure and properties which has the purpose of outlining the state of the art at present.

3.1 *TOUGHENING AND STRENGTHENING MECHANISMS*

The theory of toughening and strengthening mechanisms operating in zirconia-mullite have largely been worked out on other ceramic systems, in particular on zirconia, alumina and zirconia-alumina. The intensity of research on zirconia, and zirconia-alumina systems has not been matched in zirconia-mullite, and attempts to directly relate mechanisms of transformation and microcrack toughening have not proved altogether successful. Part of the problem can be attributed to difficulties inherent in testing techniques. For various reasons different toughness testing techniques can give very different results [45]. Although variations of toughness with test technique has been given some attention [45-47], this is more often than not ignored when quoting data from the literature. Under these circumstances there is a very real danger of arriving at incorrect conclusions concerning the properties of a material. Ideally a range of tests under different conditions should be conducted in order to characterize a ceramic for a particular application. This is both expensive and time consuming and is thus rarely carried out. Variation in toughness data is generally small for zirconia-mullite when compared to zirconia-aluminas and this reduces the importance of this particular problem.

Strength tests pose a different set of considerations when comparing data from different sources. Considerable differences in results can be achieved through variation in sample dimensions and testing geometry. For example 3-point bending usually gives 20-30% higher strength figures than 4-point bending. It is therefore, important to consider carefully the relevance of test technique to the end-use of the material or problem being studied.

A number of toughening mechanisms have been proposed in ceramic materials. These have mostly been studied in specific materials where a particular mechanism is clearly dominant. The situation with zirconia-mullite is more ambiguous for two apparent reasons. Firstly, there is a considerable range of microstructures and compositions covered under the term 'zirconia-mullite', and secondly toughening may result from several interacting mechanisms with none clearly dominant.

The best known toughening mechanism operating in zirconia systems is that due to transformation toughening which has received an immense amount of interest and has been widely reviewed [6,48-53]. Considerable research and discussion has also been focused on microcrack toughening [1,54-56]. In zirconia systems these two mechanisms tend to dominate the properties. Other less important mechanisms also exist such as crack deflection toughening. The dispersion of a second phase in a ceramic matrix results in complex stress fields due to thermal and elastic mismatch. These stress fields interact with that surrounding a crack and can result in a toughening increment. This has been studiud by Lange [57]. General microstructural considerations such as crystal type, shape, size and orientation also play a role.

Wallace *et al.* [58] have shown that transformation toughening is effective in zirconia-mullite (*Fig. 28*). *They found that the unusual* microstructural development involved in reaction-sintering formed round zirconia particles which resulted in the tetragonal phase being stable with a particle size of up to approximately 1,[illegible] µm. This compares with a maximum of approximately 0,6 µm in sintered composites such as undoped zirconia-alumina.

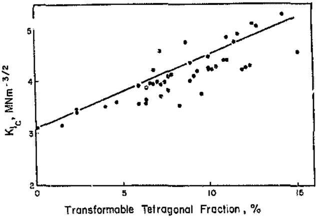

FIGURE 28: Measured fracture toughness of reaction sintered zirconia-mullite as a function of transformable tetragonal zirconia, after Wallace *et al.* [58]

Grain boundary toughening due to the presence of solid solutions has been proposed by Moya and Osendi [12,27] in sintered zirconia-mullite. A thermodynamic mechanism was proposed [59] involving an elastic energy term related to the solid solution interface between zirconia and mullite grains as determined by TEM [28]. It may be argued that this toughening mechanism is similar to crack deflection toughening.

More recently microcracking and twinning of transformed zirconia has been shown to exist in doped [42] and stoichiometric [60] zirconia-mullite. Twinned crystals tend to exhibit a certain degree of debonding between grain and matrix. This suggests toughening in these systems to be microcrack related.

The examples of toughening mechanisms described above have been studied on zirconia-mullites processed by very different routes. Some aspects of processing and the effects on properties will be discussed in the next section.

3.2 THE EFFECT OF PROCESSING ON PROPERTIES

3.2.1 *Influence of dopants*

The most extensive work on the effect of dopants in the ZrO_2 - mullite system has been undertaken by Pena *et al.* [29-31] using CaO, MgO and TiO_2. Their results are summarized in Table 4. The dopants were added stoichiometrically so as to form spinel, aluminium titanate and anorthite respectively for MgO, TiO_2 and CaO, as minor phases in a ZrO_2-mullite ceramic.

TABLE 4: Effect of dopants on ZrO_2-mullite properties drawn from refs [29-31]

Minor Phase	Vol %	σ_f (MPa) 3-point	K_{Ic} (MPa.$m^{½}$)	Firing Temp. (C)	Time (Hrs)
Spinel	6,4 18,6	329 258	4,6 4,5	1 500 1 450	0,25 1,5
Aluminium Titanate	6,2 20,8	310 250	4,9 4,7	1 500 1 500	1 2
Anorthite	15,1 29,6	270 235	4,4 4,3	1 450 1 450	2 2

The volume percent of minor phase present in the sintered product has a strongly deleterious effect on strength as is illustrated in Fig. 29. This is a major disadvantage of using liquid phase

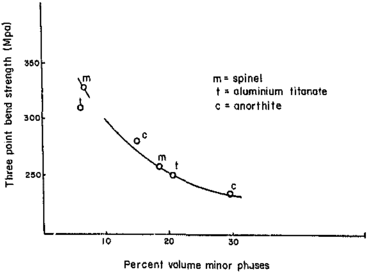

FIGURE 29: Plot of strength versus volume percent of minor phase

sintering which is primarily employed to lower sintering temperature and hence reduce production costs. In these materials no relationship was observed between the tetragonal zirconia content and strength or toughness which differentiates them from the undoped material studied by Wallace *et al.* [58] (Fig. 28).

The only other dopant reported in the literature in this system has been Y_2O_3. This work by Joliet *et al.* [61] showed that the addition of yttria increased the amount of mechanically transformable zirconia. However, toughness remained constant below 5 wt.% Y_2O_3 addition and then decreased. This also supports the view that transformation toughening may be of only marginal significance in doped zirconia-mullite. The variation in Young's modulus and porosity in the materials examined indicated substantial microstructural variation which could have masked effects due to tetragonal zirconia. Also the method of measuring toughness was by Vicker's indentation which tends to give artificially high toughnesses *in porous materials which adds another potential* source of variation. The hardness results reported were very low at 4,5 - 6,0 GPa compared to 12,6 GPa reported for undoped zirconia-mullite [15].

3.2.2 *Variation of stoichiometry*

The stoichiometry of reaction sintered zirconia-mullite can be varied by adding either silica, or excess zircon or alumina. By manipulating the stoichiometry in this way Orange *et al.* [16] studied the properties of three zirconia-mullite mixes, two of which had varying quantities of residual alumina. The materials *were all sintered in a single step process* with 1,8 wt.% magnesia added as a sintering aid. The sintering details and mechanical properties are summarized in Table 5.

TABLE 5: Processing and properties of data for various zirconia-alumina-mullites (from Orange *et al.* [16])

Composition	Vol.% of phases present	Sintering temp. (C)	Sintering (Hrs)	σ_f (MPa)	K_{Ic} (MPa.m$^{1/2}$)
1	75% mullite 25% ZrO_2	1 500	0,25	270	4,6
2	56% mullite 26% Al_2O_3 18% ZrO_2	1 500	0,5	315	4,75
3	11% mullite 72% Al_2O_3 17% ZrO_2	1 500	2	330	5,25

Composition 1 clearly showed the effects of liquid phase sintering with mullite needles in excess of 10 microns long with rounded zirconia particles both inter- and intragranular. This differed greatly from compositions 2 and 3 which showed faceted inter- and intragranular zirconia with faceted mullite and alumina, with an average grain size of 3 and 2 microns respectively. Composition 2 tended to have larger more rounded grains than the high alumina material. The large grain size of the stoichiometric composition occurred despite a very short sintering time.

A fractographic study of four zirconia-mullite-aluminas showed that different fracture behaviour and microstructure could be engineered with materials of identical chemical compositions [43]. The materials were processed according to the stoichiometry of the equation

$$\begin{aligned} 2ZrSiO_4 + 0{,}3(MgO + Al_2O_3) + 7{,}4Al_2O_3 \rightarrow \\ 2ZrO_2 + 3Al_2O_3.2SiO_2 + 0{,}3MgO.Al_2O_3 + 3{,}4Al_2O_3. \end{aligned} \qquad (10)$$

The microstructure was modified by varying the dopant using either spinel or magnesia, and varying the sintering time. The mechanical properties are reproduced in Table 6. The choice of lower sintering time was due to larger volumes of lower-viscosity liquid phase which can form at low temperatures due to possible $MgO-SiO_2$ phase formation.

TABLE 6: Mechanical properties of zirconia-mullite-alumina after Baudin *et al.* [43]

Sample No.	Dopant	Sintering Time (mins)	Toughness ($MPa.m^{1/2}$)	Strength (MPa)	Weibull Modulus
1	Spinel	120	4,3 ±0,4	316 ±33	9
2	Spinel	210	4,1 ±0,2	273 ±26	7
3	Magnesia	90	3,9 ±0,2	341 ±33	12
5	Magnesia	180	4,2 ±0,2	314 ±26	10

Two general observations from the data are that the magnesia doped material produces ceramics with higher strengths, as does lower time of sintering. The strength and toughness of these materials appeared to be due to microcracking and crack-deflection. The contribution of zirconia seemed to be strongly related to the nature of the grain boundaries. The magnesia-doped material showed the existence of a continuous composition change across grain boundaries whereas the spinel-doped material showed microcracking phenomena around the zirconia boundaries suggesting the presence of glassy phases. The higher strength of the magnesia, low-time-sintered material was attributed to the absence of microcracks with crack-deflection as the toughening mechanism.

The reduction in strength with time of sintering suggests that equilibration of phases may result in a growth of intergranular glassy phases due to impurities. In addition the longer sintering times will result in a larger average grain size which will also be deleterious to properties. The presence of excess alumina probably has a number of effects namely, preventing excessive liquid phase formation, inhibiting mullite grain growth, while acting as stress concentrators and microcrack initiators.

The two papers discussed in this section support evidence of a multi-factor toughening mechanism in zirconia-mullite and suggests better properties can be achieved with excess alumina with the zirconia-mullite reaction.

3.2.3 *Other factors affecting processing*

Processing reaction-sintered zirconia-mullite involves the interaction of a great number of factors, most of which have been studied at one time or another although few have been studied together. A typical approach used in investigating the zirconia-mullite system is to study the effect of either stoichiometry or dopant concentration, along with sintering temperature and time, against either properties or microstructure. Probably the most systematic study of this nature was by Leriche *et al.* [62] who studied the effect of magnesia content, firing temperature and time on the densification degree of reaction and microstructure of reaction sintered zirconia-mullite. They found the optimum magnesia content to be between 1 and 2% with higher contents hindering mullite crystallization. Increasing time, temperature and magnesia ultimately leads to substantial zirconia and mullite grain growth. Zirconia grain growth was shown to occur by a dissolution-precipitation mechanism.

The particle size of the alumina powder can have a major effect on the sintering behaviour of zirconia-mullite. Moya et al. [63] studied the effect of a 0,5 µm and 3,6 µm average particle size alumina in calcia and magnesia doped materials. They found that the finer alumina compacts showed excessive grain growth and liquid exudation to the surface. This did not occur with compacts containing excess alumina.

3.3 *SUMMARY AND BACKGROND TO EXPERIMENTAL DESIGN*

3.3.1 *Summary*

Processing trends in this system have developed, favouring doped routes usually involving calcia and magnesia although titania and yttria have also been studied. Liquid phase sintering, unless carefully controlled, can result in excessive mullite and zirconia grain growth. This can be controlled by varying particle size, temperature and time of sintering, amount of dopant and stoichiometry particularly in the form of added alumina.

Toughening and strengthening mechanisms have been evaluated and although transformation toughening has been demonstrated, the consensus of opinion is that this is unimportant relative to other mechanisms. These are believed to be a combination of microcrack toughening and microstructural effects such as stress concentration points and grain boundary phases. Over-sintering can occur and results in poorer properties probably due to relief of internal stresses or increasing glassy phases at grain boundaries or a combination of the two.

3.3.2 *Background to Experimental Design*

Extensive use has been made of statistical experimental design techniques during the course of this investigation. These were based on factorial designs, response surface methods, multi-factor analysis of variance and component estimation methodology. An extensive bibliography [64-70] and standard computer techniques were used in support. The latter specifically used the Quattro spread sheet package (1987 version) by Borland International for data manipulation and Statgraphics (version 2.6) by STSC Inc. for statistical analysis and graphics generation.

Classical research, in determining the effect of variables on a measured parameter, is based on the one-parameter-at-a-time (OPAAT) method. This method, in which experimental factors are varied one at a time, with the remaining factors held constant, was formerly regarded as the only correct way to conduct research. This approach provides an estimate of the effect of a single variable at a selected fixed point in a multivariable space. However, for such an estimate to have any general relevance, it is necessary to assume that the effect would be the same at any other point in the multivariable space. In reality, this is rarely the case. As a result there has been growing interest in the design and analysis of multiparameter experiments, which allows greater depth, precision and comprehensiveness to be attained in research.

Multiparameter experiments based on factorial designs have the following advantages over 'OPAAT' methods.

- For statistical reasons they determine the effect of variables with greater precision for a given number of runs. For example a factorial experiment requires eight runs to measure the effects of three parameters, whereas an 'OPAAT' design requires 24 runs to attain the same precision.
- They can detect and measure interactions between variables in a manner not possible for 'OPAAT' designs.

- They provide a means of quickly optimizing or minimizing a desired parameter by suitable manipulation of variables, a task that is difficult for 'OPAAT' designs.
- The data obtained from factorial designed experiments is in a format which is ideal for computer aided mathematical modelling and statistical analysis.

A particular characteristic of the data produced in experimental designs is often the appearance of, for example, poor mechanical properties which would not normally be taken into consideration in classical experimental procedures. This data is, however, critical in directing the course of further experimentation. The power of the technique lies in the phenomenon that no information is wasted.

The central feature of the techniques is the principle of orthogonality. Orthogonality in experimental design enables several parameters to be investigated in a carefully designed experiment so that information about each is unambiguous when analysed. Many designs are available with varying degrees of complexity and are collectively termed orthogonal or factorial designs. One special feature of factorial designs is that they also provide quantitative information on parameter interactions which is often critical to understanding complex systems. The basis of these techniques was developed by Fisher [70] in the 1920's while working on increasingly complex agricultural field trials laid at Rothamsted and elsewhere in England. Typical problems being studied were experiments comparing the yield from several varieties of wheat. In experiments of this nature it was difficult to separate the effects of the different wheat varieties from other important factors such as weather conditions, type of soil, position in field and variances in fertilizer and minerals among others. Another difficulty was separation of experimental error due to extraneous variations due to the parameters being investigated. While studying these problems Fisher laid down the basis of analysis of variance which has since found applications in a wide variety of fields.

The use of orthogonal designs has particularly been developed in China and Japan in recent years for experimental optimization and is considered to be a major factor in the success of Japanese quality control groups. Yin and Jillie in a recent paper [71] emphasized the lack of awareness of these methods in America which would severely limit competitive efficiency. The probable reason for this is the extreme rigidity with which orthogonal designs tend to be treated in the West which restricts usage to the domain of statisticians. There is, however, a heuristic approach which can be used to encourage experimenters to design more complex and realistic experiments, while avoiding the involvement of rigid statistical assumptions. Certain simple precautions can be taken such as the use of reverse Yates algorithm for residual analysis [72] to check for errors and the use of normal probability plots to check data. The greatest drawback of using this approach is that an injudicious design may result in a great deal of time wasting. Chatfield [68] in his chapter on "planning the experiment" particularly emphasizes that careful planning in conjunct of a good knowledge of the system is essential prior to laun into experimental design. It is useful, however, to use . two- or three-parameter experiments to build up this knowledge and to aid in selecting the more important parameters for optimization.

These comments on the experimental approach adopted are expanded in Appendix A with appropriate examples for readers unfamiliar with factorial design methodologies.

SECTION 2: EXPERIMENTAL, RESULTS AND DISCUSSION

4. EXPERIMENTAL DESIGN AND METHODOLOGY

The purpose of this study is to determine the feasibility of replacing debased aluminas with zirconia-mullite for abrasive wear resistant applications. In order to be competitive the processing conditions are constrained within the limits set by debased alumina manufacture. As a result the objectives can be specifically defined.

4.1 *OBJECTIVES*

These can be considered in two groupings, namely target material properties and processing limitations. The former are listed in Table 7.

TABLE 7: Summary of physical properties of current commercial alumina

Property	*Units*	Results
Bulk Density	g/cm^3	3,5 - 3,6
Wear	mg/g SiC cm^3/particle impact	0,41 $4,1 \times 10^{-10}$
Strength	MPa	207
Weibull Modulus	-	30
K_{Ic} (indentation)	MPa.m$^{1/2}$	<2,5
H_V	GPa	10 - 11
Young's Modulus	GPa	270

The production limitations are essentially those that apply to current commercial alumina tile manufacture. These are outlined in the production flow chart in Fig. 30. Any laboratory development work should be essentially equivalent to the production technology, or be as close an approximation as available facilities allow.

4. EXPERIMENTAL DESIGN AND METHODOLOGY

The purpose of this study is to determine the feasibility of replacing debased aluminas with zirconia-mullite for abrasive wear resistant applications. In order to be competitive the processing conditions are constrained within the limits set by debased alumina manufacture. As a result the objectives can be specifically defined.

4.1 *OBJECTIVES*

These can be considered in two groupings, namely target material properties and processing limitations. The former are listed in Table 7.

TABLE 7: Summary of physical properties of current commercial alumina

Property	*Units*	Results
Bulk Density	g/cm^3	3,5 - 3,6
Wear	mg/g SiC cm^3/particle impact	0,41 $4,1x10^{-10}$
Strength	MPa	207
Weibull Modulus	-	30
K_{Ic} (indentation)	$MPa.m^{1/2}$	<2,5
H_V	GPa	10 - 11
Young's Modulus	GPa	270

The production limitations are essentially those that apply to current commercial alumina tile manufacture. These are outlined in the production flow chart in Fig. 30. Any laboratory development work should be essentially equivalent to the production technology, or be as close an approximation as available facilities allow.

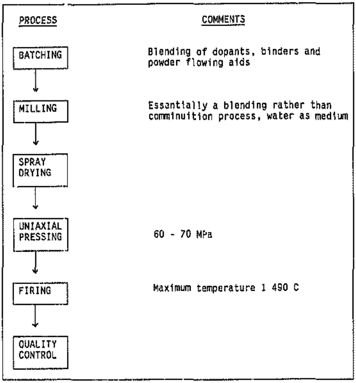

FIGURE 30: Production flow chart and comments

There were four major differences between the laboratory and production processes, namely at the milling, drying, pressing and firing steps. Milling in the production environment was a blending rather than a comminuition step in a ball-mill, whereas in the laboratory milling was used to vary particle size in an attrition mill.

The second difference was in the drying of milled powders. There were no spray-drying facilities capable of the output required in the laboratory so conventional batch oven drying, followed by sieving, was used. This resulted in laboratory powders with much poorer flow properties when compared to production powders. Spray-drying also permitted the use of suitable additives such as waxes which aided the flow properties. This was not feasible with oven drying owing to homogeneity and powder agglomerate shape differences.

The third difference was in the nature of the presses. The production press has an automatic powder feed and uniaxial action capable of reaching pressures of 60 - 70 MPa. In the laboratory uniaxial pressing of 2 - 10 MPa was followed by cold isostatic pressing to a pressure of 200 MPa. Any major differences due to the two methods were discounted by a simple comparative test. Ceramics produced by pressing spray-dried alumina powder using both techniques had the same densities and microstructures.

The final difference was in the nature of the firing cycles. These differed considerably in time. These are reproduced in Table 8. Once again, any major differences were discounted by comparing densities and microstructure of tiles fired using both cycles.

TABLE 8: Firing cycles for production and laboratory processing

PRODUCTION			LABORATORY		
Heating Rate (C/hr)	Soak Temperature (C)	Soak Time (hrs)	Heating Rate (C/hr)	Soak Temperature (C)	Soak Time (hrs)
100	500	1	300	500	1
150	1 490	5	300	1 490	2
150	800	0	300	30	end
300	30	end			

4.2 *EXPERIMENTAL*

Based on the material and processing objectives and limitations outlined in the previous section, the following generalized experimental techniques were used.

4.2.1 *Processing*

For powder processing one of two attritor mills were used dependent on the mass of powder required by the experiment. Both mills were Netzsch Molinex laboratory attritors of the same general design and differed only in their capacity. The smaller mill had a charge capacity of 250 g of powder and 1 200 g of 2 mm diameter zirconia milling beads to which was added typically 150 ml distilled water and 2 wt.% 200 Mwt polyethylene glycol as a binder. The larger mill had a charge capacity of 1 500 g and 6 kg of the zirconia milling media. Added to this was typically 1 to 1,75 ℓ of distilled water and 2 wt.% polyethylene glycol.

Four powders were used depending on the purpose of the experiment. These are listed in Table 9 with specifications in Tables 10 and 11.

TABLE 9: Powders used during experimental work

POWDER	Zircon		Alumina	
Grade	Ferro 2 micron	Ferro Superfine	BACO MA4LA	ALCOA A16SG
Average Particle Size (µm)	2,8	0,66	5,5	0,34
Source	Ferro Industrial Products, Brakpan, SA Mined by Richard's Bay Minerals, Richards Bay, Natal, SA		BA Chemicals Ltd, Chalfont Park. Gerards Cross, Buckinghamshire, England	Aluminium Co. of America, Pittsburgh, Pa

TABLE 10: Chemical analysis as provided by suppliers

Type	Zircon		Alumina	
	2 micron	superfine	BACO MA4LS	ALCOA A16SG
% Al_2O_3	0,12	0,12	99,7	99,5
% ZrO_2	65,9	65,9	-	-
% SiO_2	32,0*	32,0*	0,05 - 0,07	0,03 - 0,07
% Na_2O	-	-	0,02 - 0,04	0,08 - 0,1
% Fe_2O_3	0,08	0,08	0,02 - 0,04	0,01 - 0,03
% CaO	0,09	0,09	0,02 - 0,05	-
% MgO	0,02	0,02	-	-
% Loss on ignition	0,20	0,20	0,1 - 0,2	-

Approximately 0,4% as free SiO_2

The powders were milled for 1-6 hours and then oven dried for 3 hours at 130 C followed by 3 hours at 80 C. This ensured a consistently dried powder and avoided carbonization of the binder. The dried powders were then granulated through a 600 µm sieve followed by a 300 µm sieve.

Green compacts were formed by uniaxial pressing to a pressure of 2-10 MPa dependent on the size of compact. The size and shape of compacts with respect to the nature of tests to be conducted on each are summarized in Table 12. Once formed the compacts were cold isostatically pressed at 200 MPa.

The compacts were fired in a Carbolite RHF16/10 furnace controlled by a Eurotherm Type 818 Programmer.

TABLE 11: Particle size analysis

Particle size (microns)	Cumulative percent mass passing through			
	ZIRCON		ALUMINA	
	2 micron	superfine	BACO MA4LS	A16SG
42,21	100,0	100,0	100,0	100,0
29,85	100,0	100,0	100,0	100,0
21,10	100,0	100,0	100,0	100,0
14,92	100,0	100,0	95,1	100,0
10,55	100,0	100,0	83,4	100,0
7,46	87,3	100,0	63,5	100,0
5,27	77,4	100,0	39,8	100,0
3,73	71,8	100,0	26,7	100,0
2,63	56,4	89,3	14,3	100,0
1,69	52,6	82,3	11,6	100,0
1,01	46,4	68,2	8,5	98,8
0,66	37,0	63,2	6,6	86,0
0,43	28,3	39,6	6,6	69,5
0,34	17,8	24,4	4,9	45,8
0,24	10,5	14,3	2,6	28,0
0,17	5,5	7,5	1,3	14,5

Analysed by Microtrac, small particle analyser (SPA) Model 7995-30.
Manufactured by Leeds & Northrop Instruments.

TABLE 12: Sample dimensions

Nature of test	Height (mm)	Width (mm)	Length (mm)	Diameter (mm)	Uniaxial pressing pressure (MPa)
Density Apparent prosity Young's modulus Hardness Toughness Microstructure	10	-	-	17	3
Modulus of rupture	8	8	80	-	5
Erosion wear	8	-	-	45	10
X-ray diffraction	1	-	-	22	2

4.2.2 *Measurement of Properties*

4.2.2.1 *Density and apparent porosity*

Samples were first weighed dry (to 0,0001 g) on a Mettler AE160 balance. They were then subjected to vacuum in an empty dessicator for 15 minutes. Vacuum was provided by a conventional oil vacuum pump. Water was then admitted to cover the specimens and then vacuum was released. The samples were then first weighed while immersed in water and then reweighed with any absorbed water, care being taken to remove surface moisture. From the dry (A), immersed (B) and wet (C) weights the density and apparent porosity can be calculated according to the equations,

$$\text{\% Apparent Porosity} = \frac{(C - A)}{(C - B)} \times 100 \qquad (11)$$

$$\text{Density (g/cm}^2\text{)} = \frac{A}{(C - B)} \qquad (12)$$

4.2.2.2 *Hardness and Toughness*

Hardness and toughness measurements were carried out on polished surfaces. Hardness tests were done using a Vickers square-pyramid diamond indenter. A typical indentation is represented in Fig. 31.

The load applied is usually between the minimum load at which $c \geq 2a$ and a maximum at which chipping occurs from lateral cracking. Loads used were typically 20 - 30 kg. The indentation diagonal and crack lengths were measured using a Polyvar optical microscope using a standard graticule. Hardness (GPa) was calculated using the equation

$$H_v = 0{,}47 \frac{P}{a^2} \tag{13}$$

where P = load (N) and a is half the indentation diagonal (m).

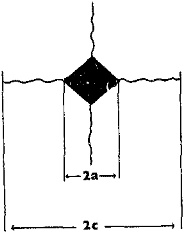

FIGURE 31: Vickers indentation and crack geometry

Toughness measurements were carried out using the same indentations, but measuring the length of the cracks in addition to the diagonals of the indentation. The calculation was done using the equation [73],

$$K_{IC} = 0{,}016 \left(\frac{E}{H}\right)^{1/2} \left(\frac{P}{c^{3/2}}\right) \tag{14}$$

where H is hardness (MPa), c is half the crack length (metres), E is Young's modulus (GPa) and P is load (Newtons).

4.2.2.3 *Modulus of rupture (MOR)*

MOR tests were carried out using four-point bend test with an outer span of 56 mm and an inner span of 28 mm. Samples tested had typical dimensions of typically 65 x 6 x 5 mm. Samples were loaded at a rate of 0,5 mm/min, on a JJ Instruments M100K tensile tester with a 10 kN load cell. The height and width of the test specimens were measured with a micrometer (to 0,01 mm) at the site of fracture. MOR was calculated according to the equation

$$MOR = \frac{3\,P(L-l)}{4bd^2} \tag{15}$$

where P is the breaking load (N), L is the outer span, l is the inner span and b and d are the breadth and height of the specimen respectively (m). MOR measurements are reported in GPa.

In general 15 - 25 specimens were tested to provide a representative sample of each material. The results for four-point bend tests are usually calculated using the Weibull statistical distribution, however, owing to constraints on the experimental design analysis, the normal distribution was shown to be a reasonable representation and this was used for analysis purposes. This is discussed in Section 4.4.

4.2.2.4 *Young's modulus*

Young's modulus was obtained by measuring the speed of sound of both longitudinal and transverse wave pulses through a specimen of the material under investigation. The specimen geometry was typically 15 mm in diameter and 6 mm in height. Ultrasonic wave pulses (f = ~10 MHz) were introduced into the specimen by a piezoelectric transducer bonded to it by a contact paste The paste was 1:1 glycol/phthalic anhydride. Each pulse is reflected at free surfaces of the sample with diminishing amplitude which is detected on an oscilloscope. The time lapse of the echoes is measured by super-imposing on the pulse a normalizing sine wave of variable frequency which permits overlap of consecutive echoes. For a more accurate determination the driven frequency is used to overlap one echo onto the next and then fine-tuning is possible thereby increasing precision. The distance the echo travels is simply determined by measuring the height of the sample and multiplying by two. This is referred to as the pulse echo overlap (PEO) technique and is reviewed by Papadakis [74]. The measurement procedure has been laid out comprehensively by Levitt [75]. This technique also provides the bulk modulus and Poisson's ratio. The equations used are as follows,

$$L = 4\rho l^2 f^2_{(L)} \times 10^{-6} \quad \text{(GPa)} \tag{16}$$

The distance the echo travels is simply determined by measuring the height of the sample and multiplying by two.

$$G = 4\rho l^2 f^2_{(G)} \times 10^{-6} \quad \text{(GPa)} \tag{17}$$

$$E = \frac{3LG - 4G^2}{L - G} \quad \text{(GPa)} \tag{18}$$

$$B = \frac{3L - 4G}{3} \quad \text{(GPa)} \tag{19}$$

$$\nu = \frac{L - 2G}{2(L-G)} \tag{20}$$

where

L = modulus of elasticity for longitudinal waves
G = modulus of elasticity for transverse waves
ρ = bulk density (g/cm^3)
l = thickness (mm)
$f_{(L)}$ = frequency of longitudinal waves (kHz)
$f_{(G)}$ = frequency of transverse waves (kHz)
E = Young's modulus
B = bulk modulus
ν = Poisson's ratio.

Figure 32 is a schematic of the Young's modulus apparatus.

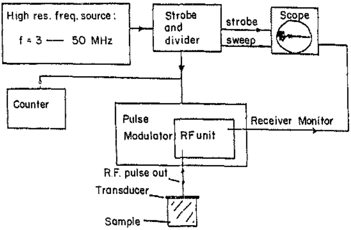

FIGURE 32: Schematic of Young's modulus apparatus after (Levitt) [75]

4.2.2.5 *Erosion by particle impact*

Erosion by particle impact was performed using the apparatus illustrated in Fig. 33. A predetermined mass of abrasive particles was fed in to an air stream by means of a vibratory particle feeder at the rate of 10 g per minute. The air pressure was maintained at 160 kPa

The tests in this study were comparative and an impact angle of 90° was maintained for all tests. The erodents used were SiC and quartz with an average particle size of approximately 120 microns.

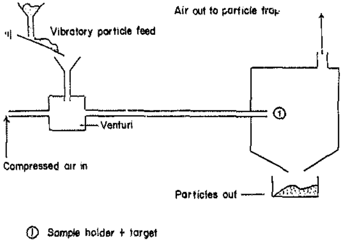

FIGURE 33: Schematic of erosion tester

4.2.2.6 *Other techniques*

Other measurements carried out were X-ray diffraction, and microstructural analysis using optical and electron microscopy. X-ray diffraction was measured using a Rigaku Geigerflex D/max 3 diffractometer, using a CuKα source and graphite monochromator. Traces were run at 0.02° per step at one step per second.

Optical microscopy was undertaken using a Reichert Univar microscope and electron microscopy was carried out using a Jeol and ISI-SX-30E scanning electron microscope with an energy dispersive X-ray spectroscope facility.

4.3 *DOPANT SELECTION*

The dopants selected for investigation were NiO, ZnO, SrO_2 and BaO. These were selected on the basis of potential similarities to MgO and CaO which have been successfully used in the zircon-alumina system and have been comprehensively studied.

The selected dopants can be divided into two families, one of which is likely to be similar in action to the Mg^{2+} ion while the other is more likely to resemble the action of the Ca^{2+} ion. Table 13 compares the key features of the two families.

TABLE 13: Comparison of properties of dopants [76]

Family Type	Ion	Ionic Radius for Co-ordination No. 6 (pm)	Availability of d-orbitals
Magnesia	Mg^{2+} Ni^{2+} Zn^{2+}	72 70 75	No or minimal d-orbital availability
Calcia	Ca^{2+} Sr^{2+} Ba^{2+}	[illegible]0 [illegible]5 [illegible]6	Full d-orbital shell available

The two groups in Table 13 can be distinguished primarily by differences in ionic radius and the availability of d-orbitals. Magnesium has an ionic size of 72 pm and no available d-orbitals.

The most likely ion to exhibit similar properties to Mg^{2+} is Zn^{2+} with an ionic radius of 75 pm and has no available d-orbitals as these have already been filled. Ions likely to exhibit similar properties to zinc and therefore also similar to magnesium are Cu^{2+} and Ni^{2+}. Nickel was selected for study.

The calcium family differ from the magnesium family by having very much larger (although not equivalent) ionic radii and having the full d-orbital shells available. Barium and strontium are in the same group (IIA) as calcium and magnesium although being very different from magnesium in behaviour. The cost and availability of barium and strontium carbonates makes them potentially suitable dopants.

4.4 *EXPERIMENTAL DESIGN AND ANALYSIS TECHNIQUES*

The background to the use of these techniques has been outlined in Section 3.3.2. A general flow-chart is presented in Fig. 34. The chart assumes a well planned experiment with a minimum of problems and is meant as a guide rather than a rule. Appendix A summarizes some of the salient points of the use of factorial design and optimization by the method of steepest ascent. For designs involving more than three parameters it is possible to use normal probability plots to determine whether any parameter or interaction effect is significant. This obviates the need for experimental replication and the use of analysis of variance and is described in Appendix A.6. For more precise studies, however, replication is necessary and the use of analysis of variance techniques and Fisher's 'F' test for probability has to be used (Appendix A.8).

An important requirement in the use of these techniques is that the order in which experiments are conducted should be randomized. This avoids the problem of experimental drift during the course of large factorial designs. The manner in which data is sampled and handled is also critical. Use is made of the central limit theorem (Appendix A.9) to justify the use of the normal distribution

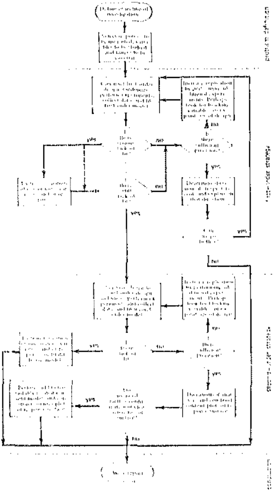

FIGURE 34: Flow chart showing basic optimization procedure from Box, Hunter and Hunter [7.]

to describe MOR data where the Weibull distribution is usually employed. The theorem is also used to increase the precision of experimental results prior to analysis of variance in certain cases.

Data from four-point bend strength tests is usually calculated on the assumption of a Weibull distribution. There are a large number of potential errors in these tests which makes the normality assumption approximately valid. This is particularly true if the samples are not all machined to the same dimensions. Since this is an expensive step it was not employed in the course of this study. An analysis of the percentage correlation of ten data sets from different samples to both normal and Weibull distributions is presented in Table 14.

TABLE 14: Percent correlation of MOR data to normal and Weibull distributions

Sample	Weibull	Normal
1	90,9	97,2
2	93,5	94,1
3	81,6	92,5
4	85,6	97,3
5	91,4	95,1
6	83,4	96,7
7	98,6	95,0
8	91,6	98,2
9	93,6	99,0
10	84,4	95,8

Only one of the ten samples showed a better fit to a Weibull distribution. The average correlation and its standard deviation for the normal distribution was 96,1% and 2,0 compared to 89,5% and 5,5 for the Weibull distribution. This supports the normality assumption for MOR data analysed in this study.

5. PRELIMINARY STUDIES

This chapter constitutes three parts. The first is a general comparison of properties and sintering behaviour of zirconia-mullite using the four selected dopants and calcia. Also included is the effect of powder particle size on sintering. The second section describes some SEM aspects of the interaction of BaO with zircon and alumina. This is followed by a quantitative factorial study of the effect of BaO on zircon.

5.1 GENERAL COMPARISON OF DOPANTS IN REACTION-SINTERED ZIRCON-ALUMINA

5.1.1 Stoichiometric zircon-alumina with 4 wt.% CaO

A mix of 4 wt.% CaO in zircon and alumina was milled with composition satisfying the equation,

$$(2+2x)ZrSiO_4 + (3+x)Al_2O_3 + xCaO \rightarrow xCaO.Al_2O_3.2SiO_2 + (2+2x)ZrO_2 + 3Al_2O_3.2SiO_2 \qquad (21)$$

The material was prepared as described in Chapter 4.2.1 using superfine zircon, A16SG alumina and Saarchem calcium oxide. The pressed powders were fired at 1 425, 1 450, 1 475 and 1 500 C respectively according to the cycle described in Table 15. XRD, density, Young's modulus, hardness, toughness and microstructure analysis were carried out on these samples.

TABLE 15: Firing sequence

Heating Rate (C/hr)	Holding Temperature (C)	Holding Time (hrs)
300	500	1
300	sintering temperature	4
300	30	-

The XRD traces for samples fired from 1 425 - 1 475 C are presented in Fig. 35. At 1 425 C the material is predominantly zircon and alumina with a small presence of zirconia and anorthite. By 1 450 C, however, the reaction is virtually complete with only a residual zircon remaining which has disappeared by 1 475 C. It was noted that where reaction was largely completed, from 1 450 - 1 500 C, a considerable quantity of liquid phase was exuded onto the sample surface. The quantity of exudation being worse with increasing temperature. The formation of excessive liquid phase was found to have a deleterious effect on microstructure through increased porosity and grain growth. This is clearly shown in Plate 2 (A and B), the most notable feature being the very large columnar mullite grains. Plate 3, shows the structure at 1 450 C which is much more dense, although the tendency of mullite to form columns can already be seen.

Figure 36 is a plot of density and Young's modulus for samples fired at different temperatures. The drop in density between 1 425 - 1 450 C is explained by the reaction products having lower density than the reactants. The drop in density from 1 475 - 1 500 C is due to a combination of excessive liquid phase formation and porosity trapping. Young's modulus follows a similar trend to density.

Table 16 summarizes the hardness and toughness data obtained. The samples fired at 1 475 and 1 500 C were unsuitable for measurement owing to severe spalling of the indentations.

TABLE 16: Hardness and toughness data

Sintering Temp. (C)	Vicker's Hardness (GPa)	Indentation Toughness (MPa.m$^{1/2}$)
1 425	11,0 ±0,2	3,5 ±0,3
1 450	9,0 ±0,2	3,0 ±0,3

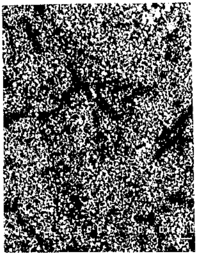

A: 400 x magnification

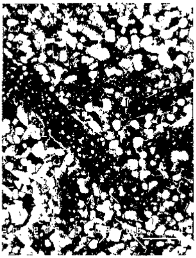

B: 1 200 x magnification

PLATE 2: Electron micrographs of CaO-doped zirconia-mullite sintered at 1 500 C

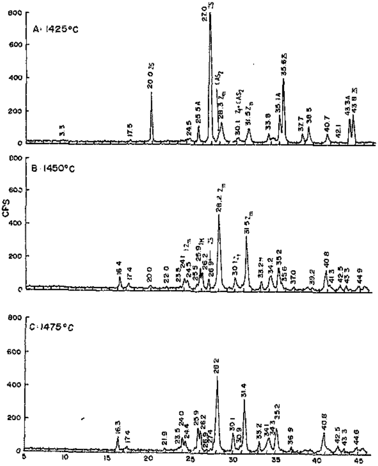

FIGURE 35: XRD traces of calcia-doped zircon-alumina sintered at various temperatures $Z=ZrO_2$, $CAS_2 = CaO.Al_2O_3.2SiO_2$, $ZS = ZrSiO_4$, $A = Al_2O_3$, $M = 3Al_2O_3.2SiO_2$

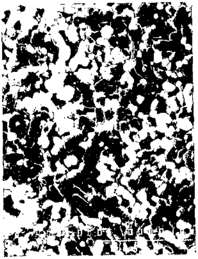

PLATE 3: Electron micrograph of CaO-doped zirconia-mullite sintered at 1 450 C. 2 000 x magnification

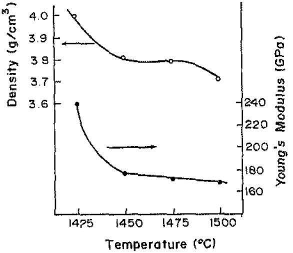

FIGURE 36: Plot of density and Young's modulus versus soak temperatures

5.1.2 *Stoichiometric Zircon-Alumina with 4 wt.% SrO*

A mix of 4 wt.% SrO in zircon and alumina was prepared, fired and tested under identical conditions to the calcia-doped material, according to the equation,

$$(2+2x)ZrSiO_4 + (3+x)Al_2O_3 + xSrO \rightarrow xSrO.Al_2O_3.2SiO_2 + (2+2x)ZrO_2 + 3Al_2O_3.2SiO_2 \qquad (22)$$

Figure 37 shows the XRD traces of the samples fired from 1 425 - 1 475 C. At 1 425 C the sample is predominantly zircon and alumina with traces of strontium aluminosilicate and zirconia as indicated. The situation is very similar at 1 450 C with possibly a slight strengthening of the zirconia peaks. By 1 475 C, however, reaction is complete. There was a noticeably lower liquid exudation in these samples with only the sample at 1 500 C showing the phenomenon. This is partly due to the higher temperature of reaction and partly to the lower molar percentage of dopant. This difference between the CaO-doped system is emphasized by the micro-graph shown in Plate 4 which at the same magnification shows a much finer microstructure, albeit predominantly zircon and alumina, than that shown in Plate 3.

Figure 38 summarizes the density and Young's modulus results, and clearly shows the effect of densification and reaction. Hardness and toughness data for the samples fired at the two temperatures representing the unreacted and fully reacted states are shown in Table 17.

TABLE 17: Hardness and toughness data

Sintering Temp. (C)	Vicker's Hardness (GPa)	Indentation Toughness (MPa.m$^{1/2}$)
1 450	11,4 ±0,2	4,3 ±0,3
1 475	8,8 ±0,2	3,1 ±0,3

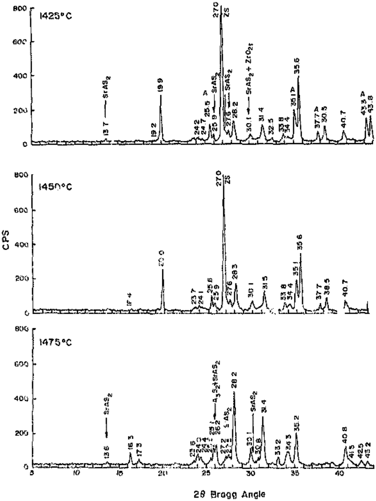

FIGURE 37: XRD traces of SrO-doped zircon-alumina sintered at various temperatures. Sr = SrO, A = Al_2O_3, ZS = $ZrSiO_4$, $SrAS_2$ = $SrAl_2Si_2O_8$

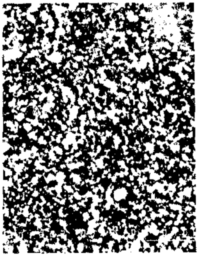

PLATE 4: Electron micrograph of *SrO-doped zircon-alumina* sintered at 1 450 C. 2 000 x magnification

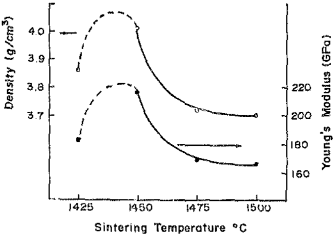

FIGURE 30: Plot of density and Young's modulus versus temperature

5.1.3 *Stoichiometric Zircon-Alumina with 4 wt.% BaO*

A mix of 4 wt.% BaO in zircon and alumina was prepared, fired and tested as for the calcia-doped material, according to the equation,

$$(2+2x)ZrSiO_4 + (3+x)Al_2O_3 + xBaO \rightarrow xBaO.Al_2O_3.2SiO_2 + 3Al_2O_3.2SiO_2 + (2+2x)\ ZrO_2 \qquad (23)$$

The soak temperatures in this case were 1 450 - 1 550 C. The XRD traces are shown in Fig. 39. At 1 450 C the material is only partly reacted with possibly barium aluminosilicate (celsian) and mullite making an appearance at 22,4 and 25,6 degrees respectively. Reaction is virtually complete at 1 475 C with the celsian making a stronger appearance. By 1 500 C, however, the celsian peak has virtually disappeared although there is little change in the zirconia and mullite peaks. In these samples there was very heavy liquid exudation from 1 475 C inclusive upwards. It was possible that the liquid exudation predominantly involving barium aluminosilicates preferentially remained a glass. To test this the samples fired at 1 450 and 1 550 C were annealed for three hours at 1 300 C in an attempt to anneal stable phases from any glass that was present. The results are shown in Fig. 40 and clearly show the appearance of celsian when compared with the traces in Fig. 39.

Plate 5 shows the microstructure of the unreacted material which can be seen to be similar to that shown in Plate 4 for the SrO-doped material. Figure 41 summarizes the density and Young's modulus results which show similar trends to the calcia and strontia systems. Hardness and toughness data for the samples representing the partially and fully reacted samples are listed in Table 18.

TABLE 18: Hardness and toughness data

Sintering Temp. (C)	Vicker's Hardness (GPa)	Indentation Toughness ($MPa.m^{1/2}$)
1 450	11,3 ±0,2	3,7 ±0,3
1 475	9,7 ±0,2	3,2 ±0,3

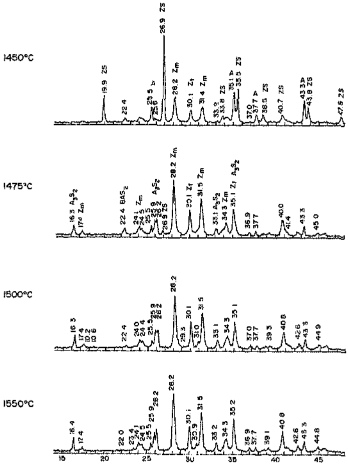

FIGURE 39: XRD traces of BaO-doped zircon-alumina sintered at various temperatures. Z_m = monoclinic ZrO_2, Z_t = tetragonal ZrO_2, A = Al_2O_3, ZS = $ZrSiO_4$, A_3S_2 = $3Al_2O_3.2SiO_2$, BAS_2 = $BaO.Al_2O_3.2SiO_2$

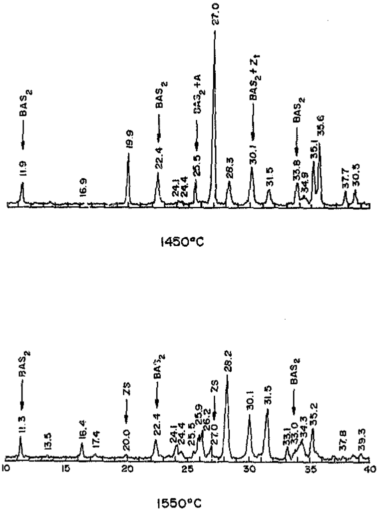

FIGURE 40: XRD traces of samples fired at 1 450 and 1 550 C after annealing for 3 hours at 1 300 C

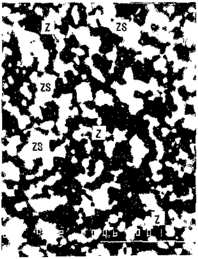

PLATE 5: Electron *micrograph (backscattered* mode) of BaO-doped zircon-alumina sintered at 1 450 C. 4 000 x magnification

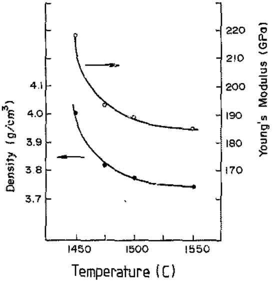

FIGURE 41: Plot of density and *Young's modulus versus sintering* temperature

5.1.4 Stoichiometric Zircon-Alumina with 4 wt.% NiO

A mix of 4 wt.% NiO was prepared and tested as for the other doped materials. The stoichiometry was according to the equation,

$$(2+2x)ZrSiO_4 + (3+x)Al_2O_3 + xNiO \rightarrow xNiO.Al_2O_3 + 2ZrO_2 + 3Al_2O_3.2SiO_2 \quad (24)$$

Samples were sintered from 1 425 - 1 500 C. The XRD traces for these are shown in Fig. 42. These show that by 1 425 C $NiO.Al_2O_3$ (spinel) had already formed although reaction only substantially occurred by 1 475 C. A noted feature of the reacted material is the more clearly defined zirconia and mullite peaks and complete lack of liquid phase exudation at all temperatures.

Figure 43 shows the density and Young's modulus behaviour with temperature. A major difference between the NiO and Group IIA dopants is continued densification after reaction. This is an unusual situation in the zirconia-mullite system and may result from enhanced ion mobility due to the presence of NiO. The lower reaction temperature (1 475 C) compared to 1 550 C for undoped material suggests that NiO has a considerable effect on ionic mobility especially as the reaction avoids excessive liquid phase formation.

Table 19 summarizes the hardness and toughness data.

TABLE 19: Hardness and toughness data

Sintering Temp. (C)	Vicker's Hardness (GPa)	Indentation Toughness (MPa.m$^{1/2}$)
1 450	7,0 ±0,2	-
1 475	8,2 ±0,2	3,6 ±0,3
1 500	10,0 ±0,2	3,1 ±0,3

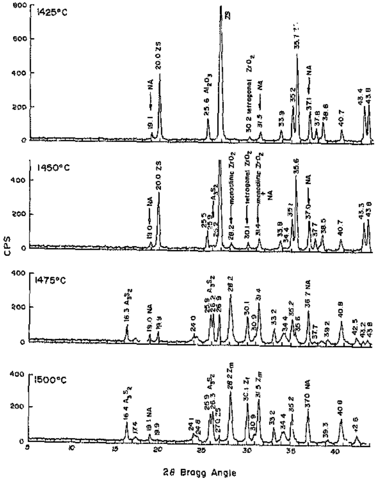

FIGURE 42: XRD traces of NiO-doped zircon-alumina sintered at various temperatures. ZS = $ZrSiO_4$, Z = ZrO_2, NA = $NiO.Al_2O_3$, A_3S_2 = $3Al_2O_3.2SiO_2$

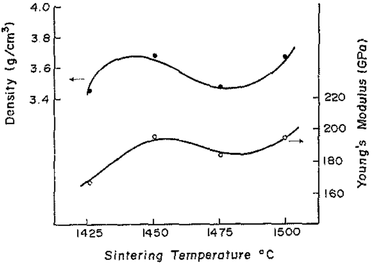

FIGURE 43: Plot of density and Young's modulus versus sintering temperature

5.1.5 *Stoichiometric Zircon-Alumina with 4 wt.% ZnO*

A mix of 4 wt.% ZnO was prepared and fired as described in Section 4.2.1. The stoichiometry satisfied the equation,

$$(2+2x)ZrSiO_4 + (3+x)Al_2O_3 + xZnO \rightarrow xZnO.Al_2O_3 + 2ZrO_2 + 3Al_2O_3.2SiO_2 \qquad (25)$$

Figure 44 shows the XRD traces of the material fired from 1 425 - 1 500 C. The traces follow a very similar pattern to those for

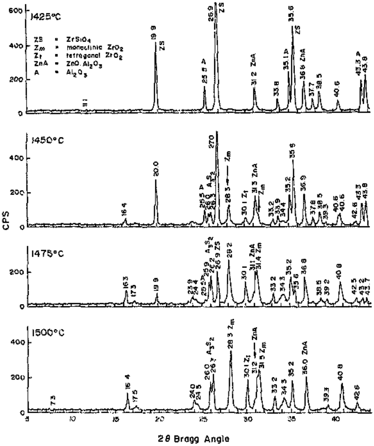

FIGURE 44: XRD traces of ZnO-doped zircon-alumina sintered at various temperatures. Z_m = monoclinic ZrO, Z_t = tetragonal ZrO_2, ZS = $ZrSiO_4$, ZnA = $ZnO.Al_2O_3$, A = Al_2O_3

NiO with reaction being virtually complete by 1 475 C. The density and Young's modulus behaviour were also similar in trend, however, the ZnO-doped material gave consistently higher figures when compared to the NiO which suggests better sintering (Fig. 45). The hardness and toughness data are summarized in Table 20 and are superior to the NiO-doped samples. The main difference between NiO- and ZnO-doped zircon-alumina appears to be in greater densification of reactants prior to reaction resulting in a generally better material.

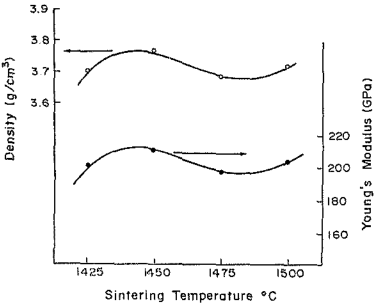

FIGURE 45: Plot of density and Young's modulus versus sintering temperature

TABLE 20: Hardness and toughness data

Sintering Temp. (C)	Vicker's Hardness (GPa)	Indentation Toughness (MPa.m$^{1/2}$)
1 450	8,6 ±0,2	4,3 ±0,3
1 475	9,4 ±0,2	4,3 ±0,3
1 500	10,5 ±0,2	3,2 ±0,3

5.1.6 *Stoichiometric Zircon-Alumina with 2 wt.% SrO and 2 wt.% ZnO*

A stoichiometric mix was prepared according to the equation

$$(2+2x)ZrSiO_4 + (3+x+y)Al_2O_3 + xSrO + yZnO \rightarrow \\ xSrAl_2O_8 + Al_6Si_2O_{13} + (2+2x)ZrO_2 + yZnAl_2O_4 \qquad (26)$$

Figure 46 shows the XRD traces of samples fired at 1 400 - 1 425 C and clearly show that reaction is virtually complete by 1 413 C. This is lower than has been reported in the literature for other doped systems. Samples fired at 1 413 C and above exhibit liquid exudation, however, they retained good hardness as is shown in Table 21. This is probably due to the very high degree of densification achieved prior to reaction (4,09 g/cm^3) forming a more cohesive structure. Figure 47 shows the density and Young's modulus behaviour with temperature.

TABLE 21: Hardness and toughness data

Sintering Temp. (C)	Vicker's Hardness (GPa)	Indentation Toughness (MPa.m$^{1/2}$)
1 400	9,8 ±0,2	4,1 ±0,3
1 413	11,2 ±0,2	3,2 ±0,3
1 425	10,9 ±0,2	3,0 ±0,3

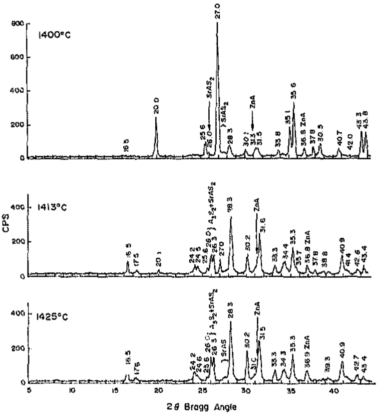

FIGURE 46: XRD traces of ZnO/SrO-doped zircon-alumina sintered at various temperatures. SrAS$_2$ = $SrO.Al_2O_3.2SiO_2$, ZnA = $ZnO.Al_2O_3$.

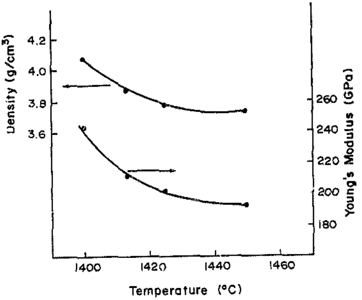

FIGURE 47: Plot of density and Young's modulus versus sintering temperature

5.1.7 *The Effect of Particle Size on Density and Young's Modulus*

Two mixes were prepared with 4 wt.% BaO according to the stoichiometry of equation (23), using two different particle size powders. The finer particle size material was made, as before, from A16SG alumina and superfine zircon having an average particle size of 0,5 µm. The coarser particle size material was made from BACO MA4LS alumina and 2 micron zircon having an average particle size of 3,4 µm. Details are contained in Table 11. The samples were fired at selected temperatures and the effects of *density and* Young's modulus plotted for each particle size as shown in Figs 48 and 49 respectively. As can be seen the effect of particle size is considerable.

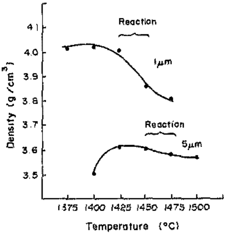

FIGURE 48: Plot of density versus temperature for two particle sizes

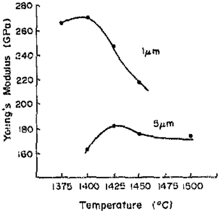

FIGURE 49: Plot of Young's modulus versus temperature for two particle sizes

5.2 *SEM STUDY OF INTERFACIAL REACTIONS*

5.2.1 *SEM Study of the Interaction of BaO with Zircon at 1 450 C*

The section describes a SEM study of the interaction of BaO with zircon and alumina in order to gain more information on the nature of the reaction, particularly in the light of the formation of liquid phases during reaction which exuded onto compact surfaces. Powder compacts were prepared as illustrated in Fig. 50. First, a loose compact of zircon was formed in a 22 mm diameter die which is represented by A in the diagram. A smaller compact of barium carbonate was formed in a 10 mm diameter die which was then placed in the centre of A, and is represented as B in the diagram. Finally, sufficient zircon was added on top of A and B and the whole section was uniaxially pressed to a pressure of 6 MPa and isostatically pressed at 245 MPa. The sample was fired for 4 hours at 1 450 C after which it was sectioned as is shown in Fig. 51.

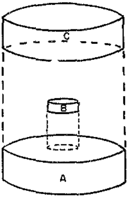

FIGURE 50: Diagrammatic representation of compact formation for interfacial reaction study

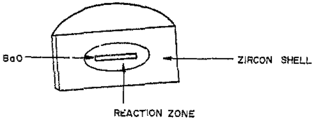

FIGURE 51: Diagrammatic representation of cut-away section of compact after firing

SEM and EDS studies were carried out on polished section of the interfacial BaO-$ZrSiO_4$ reaction zone. Firstly, eight zones were identified visually from a general micrograph (Plate 6). These zones are listed in Table 22 along with descriptions based on identified phases or notable features. Glassy phases were present in all zones in varying concentrations.

TABLE 22: Description of zones across reaction interface

Zone	Description
A	zircon - homogeneous porosity
B	zircon - inhomogeneous porosity - ZrO_2 precipitates
C	zircon - inhomogeneous porosity - fewerZrO_2 precipitates
D	ZrO_2 precipitates and crack
E	ZrO_2 precipitates and barium zirconium silicate matrix
F	Large barium zirconate crystals and barium zirconium silicate matrix
G	Fine barium zirconate crystals and barium zirconium silicate matrix
H	Barium oxide and barium zirconate

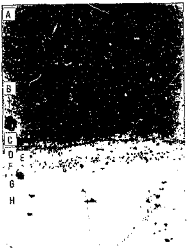

PLATE 6: General view across reaction zone

Each zone will be discussed in turn moving from the outer, barium-free zircon across the interfacial area to the inner barium oxide region. Plate 7 is a micrograph of zone A showing zircon grains (~2-5 um diameter) with fine dispersed pores and signs of darker intergranular amorphous regions. The zircon grains are largely angular. This contrasts markedly with zone B. Figure 52 shows that there is no significant difference between the EDS spectra of zircon crystals and the intergranular amorphous phase indicating that this phase is decomposed zircon *probably due to minor* impurities.

Plate 8 is a micrograph of the boundary region between zones A and B. There are four major differences between the two regions. The zircon grains in zone B are rounded; there is noticeably more amorphous phase; there are ZrO_2 precipitates; and the pore size is large. These differences become more apparent by comparing Plates 7 and 9, the latter being a micrograph of zone B. An interesting feature marked by arrows in Plate 8 is the considera-

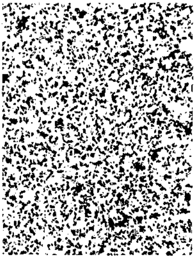

PLATE 7: Zone A: Barium free zircon

ble coarsening of zircon at the interface of the two zones. This suggests that the presence of small quantities of BaO initiates a solution-diffusion-precipitation mechanism for equilibrating the phases, concentrating zirconia precipitates on the one hand and allowing larger zircon grains to grow at the expense of the smaller grains. As the BaO concentration increases the amount of silica-rich phases will also increase and be affected by capillary forces which would sweep them away from the original reaction site. All the zirconia precipitates in Plate 9 are associated with pores or larger areas of liquid phase. Another possible cause of the porosity is grain pull-out during polishing. The removal of pores is made more difficult if they contain vapour phases which is likely to be the situation in this case.

A number of EDS scans were carried out across zone B. Figure 53 is a spectrum of one of the zirconia precipitates showing minimal presence of barium or silicon. Figures 54-56 are three spectra generated from the amorphous phase progressively deeper in to zone B towards zone C. These show that the amorphous phase is a silica-rich region with increasing barium content as zone C is approached.

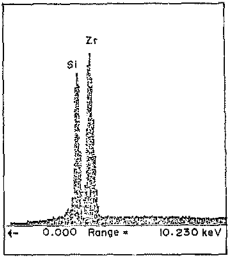

A: Spectrum of zircon crystal

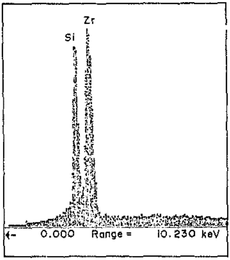

B: Spectrum of amorphous region between zircon crystals

FIGURE 52: EDS spectrum of zone A

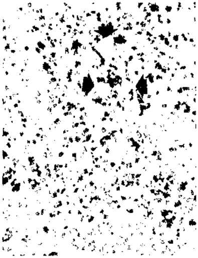

PLATE 8: Boundary of zones A and B

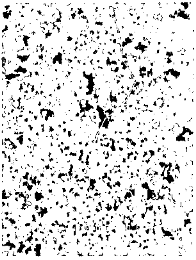

PLATE 9: Zone B

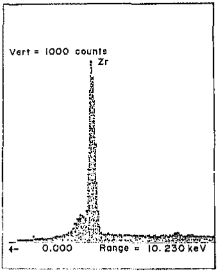

FIGURE 53: EDS spectrum of a ZrO_2 precipitate in zone B

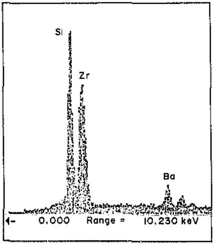

FIGURE 54: Spectrum of amorphous phase at interface between zones A and B

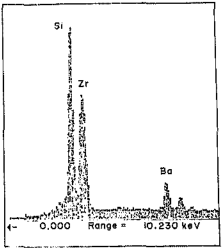

FIGURE 55: Spectrum of amorphous phase in the middle of zone B

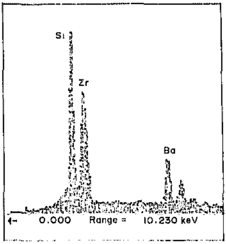

FIGURE 56: Spectrum of amorphous phase in zone B close to zone C

Zone C is a region of zircon and ZrO_2 precipitates being distinguished from zone B by the reduced amount of ZrO_2 precipitates and amorphous phase. Zone C is the culmination of a gradual change across zone B as is shown in Plate 10 where three regions have been marked. Region 1 shows clearly the presence of amorphous phase; this is substantially reduced in region 2; and finally is reduced still further along with a reduction in zirconia precipitates in region 3 which is synonymous with zone C.

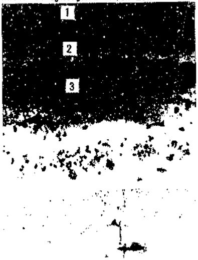

PLATE 10: 200 x magnificantion of the reaction interface showing graded changes across zone B to zone C

Zone D is an area of ZrO_2 precipitates bordering an interfacial crack formed by stress induced by melt solidification on cooling. Plate 11 shows detail of zones D, E and F. Zone E is essentially the same as D, differing only in the size of ZrO_2 precipitates which are present. Figure 57 is a spectrum of the melt in zone E from which the ZrO_2 inclusions presumably precipitated during cooling. The melt composition does not relate clearly to any known compound, the only two barium-zirconium silicates being respectively $BaO.ZrO_2.3SiO_2$ and $2BaO.2ZrO_2.3SiO_2$.

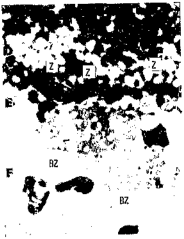

PLATE 11: 1 200 x magnification of eutectic region Z = ZrO_2; ZS = $ZrSiO_4$; BZ = $BaZrO_3$

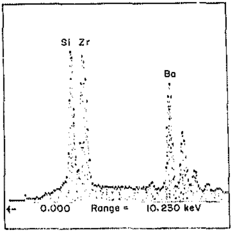

FIGURE 57: EDS spectrum of amorphous matrix phase in zone E

Zone F is characterized by angular crystals in an amorphous matrix. Figures 58 and 59 are the EDS spectra of the matrix and crystals respectively. The matrix shows a substantial change from the matrix of zone E, having a greatly increased barium content with a large reduction in zirconium. As with the matrix in zone E it does not clearly relate to any known compound, having an approximate BaO:SiO_2:ZrO_2 ratio of 3:2:1. The crystals can be identified as barium zirconate.

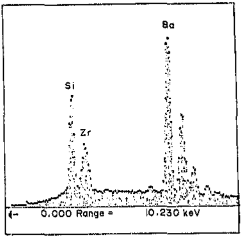

FIGURE 58: EDS spectrum of amorphous matrix phase in zone F

Plate 12 is a micrograph of the region from zone F across G to H. It can be seen that zone G is a natural progression from F, the main difference being that the crystals are finer with a narrower size distribution. Figure 60 is a general EDS of zone G and shows a substantial overall reduction of silica. This can be compared with the general spectrum of zone H which shows a large reduction in zirconia (Fig. 61). Plate 13 is a more detailed micrograph of zone H showing the inter-penetration of the barium-zirconate crystals as confirmed by EDS in Fig. 62.

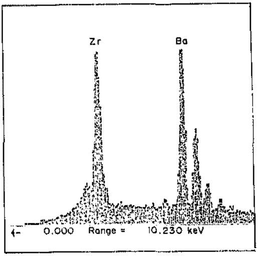

FIGURE 59: EDS spectrum of barium-zirconate crystals in zone F

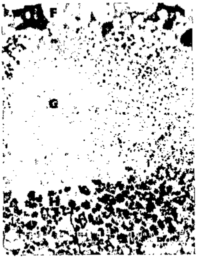

PLATE 12: 1 000 x magnification of zones F - H

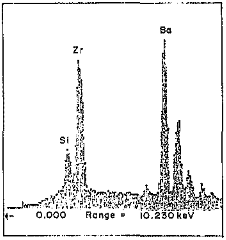

FIGURE 60: General EDS spectrum of zone G

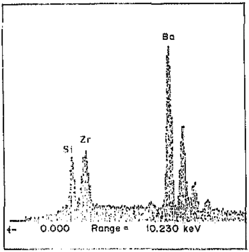

FIGURE 61: General EDS spectrum of zone H

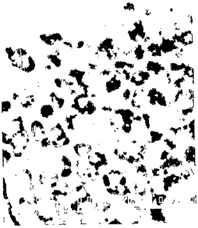

PLATE 13: 2 400 x magnification of zone H

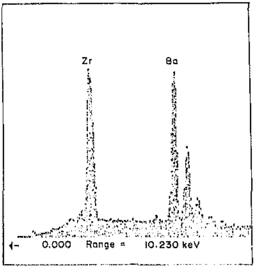

FIGURE 62: EDS spectrum of pale region in zone H

Closer examination of plate 13 shows that the dark regions are non-homogeneous. EDS spectra of this region shows two different phases as shown in Figs 63 and 64. Figure 63 is consistent with barium-oxide with a slight zirconia and silica impurity while Fig. 64 approximates the formula $2BaO.ZrO_2$.

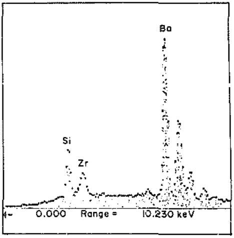

FIGURE 63: EDS spectrum of region showing BaO with impurities in darker region of zone H

This completes a descriptive overview of the macroscopic interfacial reactions between zircon and barium oxide at 1 450 C. It is clear that the presence of barium oxide causes the decomposition of zircon, initially to form an amorphous barium zirconium silicate with zirconia precipitates. The formation of this barium zirconium silicate which is liquid at 1 450 C traps large pores which which cannot be sintered out.

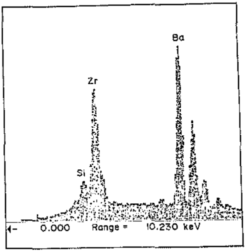

FIGURE 64: EDS sectrum of region approximating the formula of 2BaO.ZrO_2 in lighter regions of zone H

Figure 65 shows the relative concentrations of barium across the interface which is the region of interest in this system. In general it appears that the liquid silicates provide the medium for a counterflow of barium and zirconium ions driven by thermodynamic requirements. The formation of a eutectic at the original interface probably resulted in a capillary action drawing zirconia and silica deep into the barium oxide zone where different equilibrating conditions occurred. In order to have a clearer idea of the initial interfacial reactions, sintering at lower temperatures is necessary. This section serves to illustrate the complexity of the system and explains the lack of XRD information on samples fired at 1 450 C since the barium zirconium silicates are all amorphous after cooling.

5.2.2 *SEM Study of the Interaction of BaO with Zircon and Alumina at 1 450 C*

This section is a natural progression from Section 5.2.1. The only difference from the three phase study was in the formation of the compact. This is illustrated in Fig. 66, where A and D are the zircon shells, B is the $BaCO_3$ and C is alumina.

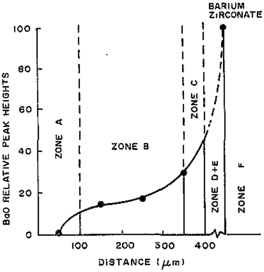

FIGURE 65: Plot of relative barium intensities across the $BaO-ZrSiO_4$ interface

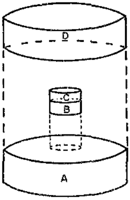

FIGURE 66: Diagrammatic representation of compact formation for four-phase interfacial study

The compact was prepared as described in Section 5.2.1 and sintered for 4 hour at 1 450 C.

Plate 14 shows a view of the alumina-zircon interface showing no substantial reaction. There are, however, a few isolated zirconia precipitates indicating some degree of zircon decomposition.

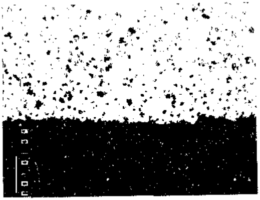

PLATE 14: Zircon-alumina interface

Plates 15 and 16 show a general and detailed view of the triple junction respectively. The dominant feature is the high degree of penetration of barium oxide into the zircon zone. This contrasts with the minimal penetration of BaO into the alumina zone clearly showing the preferential mode of action of BaO in this system.

Very little reaction was visible in the alumina zone being limited *to the edges of the alumina compact. EDS showed the formation of* celsian ($BaO.Al_2O_3.2SiO_2$), which showed columnar needle-like formation similar to mullite. All the other features were identical to those observed in Section 5.2.1 between zircon and barium oxide.

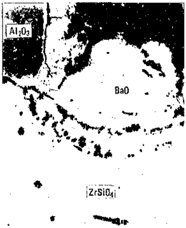

PLATE 15: General view of triple junction

PLATE 16: Detail of triple junction

Although barium oxide has a substantial effect on the decomposition of zircon it has no effect on alumina for the temperature studied. A eutectic formed by barium oxide and zircon does react with alumina as a result of a capillary action drawing the liquid into the alumina compact. No mullite was clearly identified in this system.

5.3 *DETERMINATION OF THE EFFECT OF BaO, CaO, TIME AND TEMPERATURE ON ZIRCON DECOMPOSITION AND DENSIFICATION*

The effects of BaO, CaO, sintering time and temperature on the densification and decomposition of zircon were studied using a 2^4 factorial design. This design results in 16 experimental settings as shown in Appendix A5. Each parameter being investigated was set at a high and low level as described in Table 23.

TABLE 23: Parameter level settings

Level Variable	+	-
wt.% BaO	2,0	0
wt.% CaO	2,0	0
Temperature of sintering (C)	1 450	1 350
Time of sintering (minutes)	150	30

The effects of these parameters on density, apparent porosity, Young's modulus and XRD intensities were measured. XRD diffraction intensities were measured on the 101, 200, 112 and 301 zircon reflections. These were normalized and averaged. The results are presented as normal probability plots as described in Appendix A6. These are used as they distinguish real effects from experimental error.

5.3.1 *The Effect of the Parameters on Density*

Figure 67 shows a normal probability plot of effects on density. There are two significant parameters and one significant interaction effect, all of which are positive in enhancing density. The most outstanding is temperature, with time and the dopant interaction showing a lesser effect.

5.3.2 *The Effect of the Parameters on Apparent Porosity*

Figure 68 illustrates the effect of the parameters on porosity. In this case only temperature and time are significant with temperature showing a more strongly negative effect than time. This is in agreement with the density results.

5.3.3 *The Effect of the Parameters on Young's Modulus*

Figure 69 shows the effects of parameters and interactio Young's modulus. In this case all four main parameters are significant with temperature and time showing positive effects and CaO and BaO showing negative effects. The dopant interaction is also present showing a positive effect.

5.3.4 *The Effect of the Parameters on Zircon XRD Intensities*

Figure 70 illustrates the effects of CaO and BaO on the zircon XRD intensity. Only the dopants h significant effects, namely BaO at 8% decomposition and CaO at 17%. Table 24 summarizes the weight percent and molar percent effects of the dopants. The table presents the data in terms of percent effect per percent of dopant in each case.

This shows that mole for mole BaO has a greater decomposing effect than CaO.

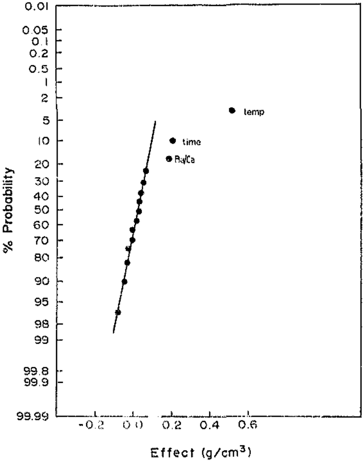

FIGURE 67: Normal probability plot of density effects

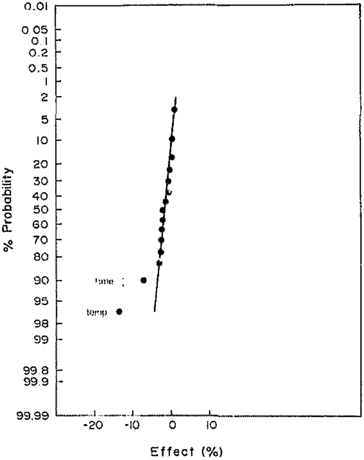

FIGURE 68: Normal probability plot of porosity effects

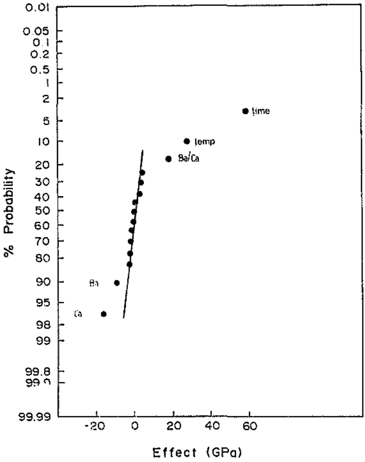

FIGURE 69: Normal probability plot of Young's modulus effects

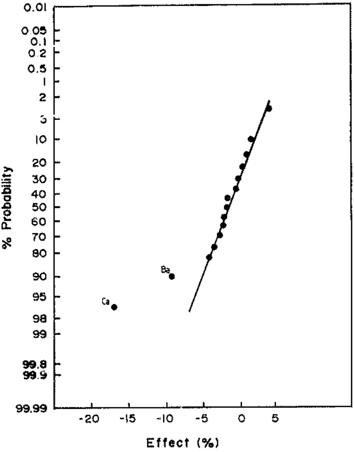

FIGURE 70: Normal probability plot of zircon XRD intensity effects

TABLE 24: Weight and molar percentage effects

	DOPANT	
	BaO	CaO
Percent effect of 1 wt.%	4	8,5
Percent effect for 1 mol.%	6,3	4,8

5.4 *SUMMARY OF PRELIMINARY STUDIES*

The preliminary studies cover a wide range of dopants and established the groundwork for a mechanistic study of the reaction process in this system. The purpose of this work was to build up a more comprehensive picture of reaction-sintered zircon-alumina under a range of conditions. Some generalizations can be drawn from the results on the dopants. The two major groups of dopants show two significant differences in behaviour. The calcia group exhibits liquid phase exudation accompanying the reaction to *zirconia-mullite whereas the magnesia group does not. The nature* of densification also differs in that the calcia group shows a general decline in density with reaction whereas the magnesia group shows an initial decline followed by an increase in density. This indicates that after reaction the zirconia-mullite continues to sinter which may be indicative of an increase in ionic mobility in the mullite in the presence of these dopants. The magnesia group shows overall poorer densities than the calcia group, which emphasizes the importance of liquid phases in sintering.

Both groups of dopants show some similarity in reducing the reaction temperature although mole-for-mole the calcia group are more effective than the magnesia group. A combination of two dopants, one from each group, showed a similar densification pattern to the calcia group, with the added advantage of a 50 C drop in reaction temperature.

In the calcia group differences were noted between members in that strontia showed a noticeably lower liquid phase exudation than either calcia or baria. Calcia and baria were shown to differ in their respective effects on the degree of decomposition of zircon in the factorial analysis. The main difference between NiO and ZnO was that ZnO resulted in higher densities than NiO.

The problem of selecting a dopant for optimization is necessarily somewhat arbitrary. The most promising material studied from the sintering perspective was the SrO/ZnO double-doped system due to the low reaction temperature. It was decided rather to study a single dopant system initially, and SrO was selected since it minimized the problematic phenomenon of liquid exudation. The excellent mechanical properties also made the SrO-doped material worthy of further study.

6. OPTIMIZATION OF SrO-DOPED ZIRCON-ALUMINA WITH RESPECT TO DOPANT, SINTERING TEMPERATURE, STOICHIOMETRY AND PARTICLE SIZE

6.1 *FIRST ORDER STRATEGY*

The first order design for optimizing SrO-doped zircon-alumina involved a 2^4 factorial studying four parameters. These were molar quantity of dopant, stoichiometry, sintering temperature and particle size. The reaction equation was

$$a\ SrO + (3+a+B)Al_2O_3 + (2+2a+B')ZrSiO_4 \rightarrow \qquad (27)$$
$$a\ SrO.Al_2O_3.2SiO_2 + BAl_2O_3 + B'ZrSiO_4 + 3Al_2O_3.2SiO_2 + (2+2a)ZrO_2$$

where $B = \frac{(|b| + b)}{2}$ and $B' = \frac{(|b| - b)}{2}$

and $a \geq 0$, $0 \geq b \geq 0$.

a and b are two independent parameters which control the stoichiometry of the equation, a is the molar quantity of SrO and b is related to the molar excess of alumina if it is positive, and zircon if it is negative.

The design for a four parameter experiment is shown in Appendix A5. The level settings are shown in Table 25.

TABLE 25: Parameter level setting

Code	Parameter	LEVEL SETTING		
		-	0	+
A	SrO dopant molar quantity (a)(moles)	0,1	0,3	0,5
B	Stoichiometry in balance (b)(moles)	-0,4	0	0,4
C	Sintering temperature (C)	1 430	1 460	1 490
D	Particle size (μm)	3,1	2,5	1,0

The material being developed was for abrasive wear resistant applications. The difficulty with optimizing on wear resistance is the time consumed in the tests and the large number of variables affecting the results. These variables include the test conditions, and the properties of the abrasive medium as well as target properties. Evans *et al.* [77] proposed the following erosion model for impact damage in the elastic-plastic response régime based on impact dynamics and fracture mechanics.

$$E = V_o^{3.2} R_p^{3.7} \rho_p^{0.25} K_c^{-1.3} H^{-0.25} \qquad (28)$$

This can be compared with the Wiederhorn and Lawn model [78] on abrasion of glass where

$$E = V_o^{2.4} R_p^{3.7} \rho_p^{1.2} K_c^{-1.3} H^{0.11} \qquad (29)$$

where V_o = particle velocity
R_p = particle radius
ρ_p = density of impacting particle
K_c = fracture toughness of target material
H = hardness of target

In both cases the important properties of the target material are hardness and toughness with hardness being more important. It was therefore decided to optimize initially on hardness. A 2^4 factorial requires 16 runs to which were added two centre points. Each run was measured three times for hardness. The results are listed in standard Yates order in Appendix B.1. Figure 71 is a normal probability plot of the calculated effects which are shown in Table 26.

The normal probability plot of effects agrees with the variance analysis in Appendix B.2. Clearly sintering temperature (C) is by far the most powerful parameter enhancing hardness, although all main parameters have a positive effect to some degree. There are two interactions which have an effect namely the dopant/temperature, and stoichiometry/temperature interactions.

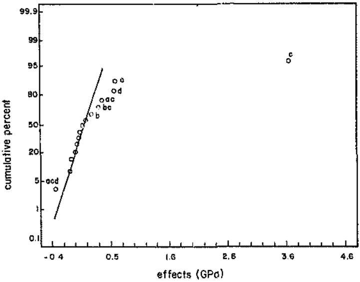

FIGURE 71: Normal probability plot of hardness effects

TABLE 26: Estimates of hardness effects

Factor	Effect	Factor	Effect
A	0,70	AD	0,02
B	0,30	BD	-0,07
AB	0,10	ABD	0,08
C	3,67	CD	-0,05
AC	0,48	ACD	-0,33
BC	0,43	BCD	0,16
ABC	0,09	ABCD	0,21
D	0,67	Average	4,99

Figure 72 is a more conventional representation of the data showing the 95% confidence intervals for factor means for all 18 runs. The centre point (runs number 17 and 18) exhibited the highest hardness of 8,8 GPa of all the runs suggesting an optimum had been straddled. A residuals analysis plot (Appendix B.3) shows fair agreement with normality.

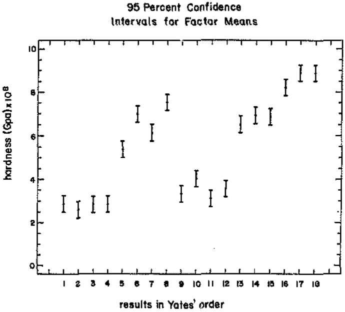

FIGURE 72: Plot of confidence intervals for hardness means versus coded parameter setting

The effect of the selected parameters on other variables was also measured. The results for Young's modulus, density and strength showed similar trends to the hardness data as indicated by the strong correlations between them. Figure 73 shows the relationship

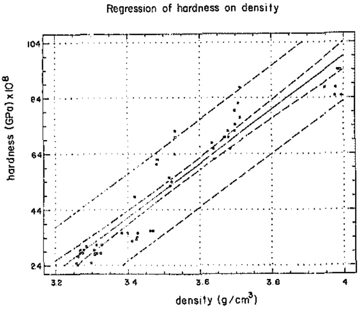

FIGURE 73: Plot of hardness versus density

between density and hardness which exhibits a 94% linear correlation. Similar relationships exist between hardness and Young's modulus, and hardness and strength with correlations of 92% and 90% respectively. The main difference in effects was that of percent dopant which had a negative effect on Young's modulus but a positive effect on the other variables. This can be understood in that the dopant would promote the chemical change from zircon and alumina to zirconia and mullite.

Toughness could not be reliably measured on these materials owing to the diversity of samples ranging from highly porous crystalline to low porosity materials containing large amounts of glassy phase as exhibited by liquid phase exudation. Toughness probably ranged from 2,5 to 4,5 $\mathrm{MPa.m^{1/2}}$.

The effects of the main parameters on the measured properties are summarized in Table 27.

TABLE 27: Effect of parameters on four properties (%)

Parameter	Hardness	Strength	Young's Modulus	Density
Percent dopant	14,1	-11,7	-18,0	2,5
Stoichiometry	6,1	- 1,7	1,8	1,0
Sintering temperature	73,5	34,5	27,8	7,9
Particle size	13,4	15,4	8,6	2,3

The effect of increasing dopant is marred by weakening the material. The increase in hardness is probably due to increasing the density but the presence of glassy phases would reduce the toughness and hence strength. The effect of stoichiometry or increasing the alumina content has a slight weakening effect and although hardness is improved this is small relative to the effects of the other parameters. The effect of decreased particle size, however, shows a reasonable improvement in both strength and hardness. Although not as powerful as temperature it provides a practical option for improving the properties given the limitations imposed by the results and production requirements.

Table 28 lists the significant interactions and their effects on the four properties being studied. All two-factor interactions and only one three-factor interaction showed some effect on at least one property. Of these only three showed an effect on hardness. The temperature/dopant interaction showed a similar effect to the dopant effect, with the increase in hardness being at the expense of strength. The interaction of temperature and excess alumina, however, showed positive effects on both strength and hardness. The three-fold interaction of temperature, dopant and particle size showed a negative effect on both hardness and strength this being the result of excessive liquid phase generation and exudation.

TABLE 28: Effect of interactions (%)

Interaction	Hardness	Strength	Young's Modulus	Density
AB - dopant/stoichiometry	-	-	-	1,1
AC - dopant/temperature	9,6	-11,2	-8,4	1,8
AD - particle size	-	-	10,2	-
BC - stoichiometry/ temperature	8,6	3,0	-	-
DB - stoichiometry/ particle size	-	2,2	-8,9	0,7
CD - temperature/ particle size	-	-2,1	-	-0,9
ACD- dopant/temperature particle size	-6,6	-5,2	-	-1,1

Table 29 lists the sum effect of increasing the parameter level when taking into account the interactions. The problem now arises as to how to improve the experiment. Although the centre point is a maximum, the hardness is only 8,8 GPa which is considerably lower than the 12,6 GPa quoted for undoped zirconia-mullite [15].

TABLE 29: Sum percent effect of increasing parameter levels

Parameter	Hardness	Strength
Percent dopant	17,1	-28,1
Stoichiometry	14,7	2,2
Sintering temperature	85,1	19,0
Particle size	6,8	10,3

These results indicate that the design was approximately central to the line or plane of optimization. This is illustrated in Fig. 74. The true optimization path lies along the line of one or in the plane of two of the axes indicated by the dotted lines. The situation is complicated by the possibility that there may be more than one possible optimization path. The most powerful effect is sintering temperature. In order to increase this substantially to attain greater hardness and strength it would eventually be necessary to reduce the dopant because of the negative effect this has both in its own right and in its interaction with higher temperatures. Owing to the magnitude of the effect of temperature this would be the favoured route for optimization if this was the only requirement. However, owing to production limitations it is not feasible to increase temperature substantially. Likewise, imbalancing the stoichiometry in favour of excess alumina could not be considered as a practical path as this would contradict the main purpose of the research.

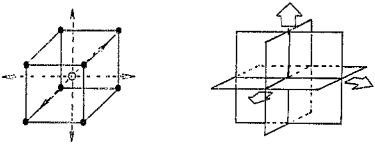

FIGURE 74: Possible optimization pa.

As a result of these considerations the least attractive path for optimizing hardness, that of decreasing the particle size, is all that remains.

6.2 *HILL CLIMBING STRATEGY*

Four mixes were prepared by milling for different times to reduce particle size. The composition and sintering conditions were the same as the centre point for the first order strategy. The results of hardness and average particle size are listed in Table 30. Figure 75 is a schematic showing the hill climbing strategy with respect to three of the parameters. Hardness figures are shown (GPa).

TABLE 30: Results of hill climbing strategy

Average particle size (µm)	2,5	1,9	1,4	1,0	0,5
Hardness (GPa)	8,8	9,3	9,7	10,2	11,2

The results show a major overall improvement in hardness as particle size is reduced. The final particle size giving a hardness of 11,2 GPa is much closer to that of 12,6 GPa for the undoped material. This illustrates an important aspect of interpreting factorial experiments. Relatively small effects may ultimately lead to major improvements in areas beyond the initial experimental region.

Milling to 0,5 µm average particle size was the practical limit of the capability of the at[illegible]or mill. It was decided at this stage to remove particle size [illegible] a parameter by using 0,5 µm powder and begin a second, first o[illegible] design based on sintering temperature, stoichiometry and percent dopant.

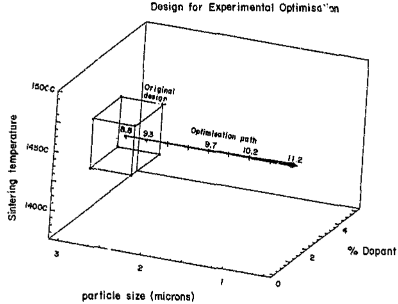

FIGURE 75: Diagrammatic representation of hill climbing strategy and results

6.3 *SECOND, FIRST ORDER STRATEGY*

The second first order design was a 2^3 factorial with level settings as listed in Table 31 below and the results are listed in Table 32. The hardness and strength data show that the centre point is once again a maximum. In order to generate a response surface of this region a second order design was superimposed on the first. The second order design for a three parameter factorial is shown in Table A.6 of Appendix A.7.

TABLE 31: Parameter levels

Code	Parameter	LEVEL SETTING		
		-	0	+
A	Dopant molar quantity (moles)	0,2	0,3	0,4
B	Stoichiometry (moles)	-0,4	0	0,4
C	Sintering temperature (C)	1 430	1 460	1 490

TABLE 32: Hardness and strength results

FACTOR AND SETTING			Hardness (GPa)	Strength (MPa)	Young's Modulus (GPa)	Density (g/cm³)
A	B	C				
-	-	-	9,98	202,4	230,6	4,09
+	-	-	8,95	197,0	222,1	4,03
-	+	-	10,00	198,9	154,2	4,02
+	+	-	9,63	205,2	217,4	4,02
-	-	+	10,24	182,6	214,4	3,94
+	-	+	9,75	185,4	193,9	3,91
-	+	+	10,12	190,5	195,7	3,86
+	+	+	9,81	199,2	197,5	3,89
0	0	0	11,2	227,6	240,0	4,11

6.4 *SECOND ORDER RESULTS*

The results for hardness as determined by multiple regression are shown in Table C.1, Appendix C.1. From the significant effects the polynomial generated is

$$\text{Hardness} = 11{,}29 - 1{,}25A + 0{,}6B + 0{,}6C + 0{,}55AB - 1{,}4A^2 - 1{,}35B^2 - 3{,}65C^2 \qquad (30)$$

where A, B and C are the coded parameters for dopant concentration, stoichiometry and sintering temperature respectively. A residuals analysis shows that the data is approximately normal and evenly distributed. These results are plotted in Figs C.2 - C.4 in Appendix C.2.

Figures 76-78 are response surface plots of hardness versus all paired combinations of the three parameters, with the third being set at zero. In all cases the results show that a maximum hardness has been straddled. Examination of the averaged data in Table C.2, Appendix C.3, shows that the centre point has a hardness of 11,3 GPa. This is the same hardness as one other point namely that fired at 1 510 C for 0,3 moles of dopant and stoichiometry set at zero. This would suggest the possibility of further optimization at higher temperatures. However, a reasonable material with acceptable hardness has been processed at 1 460 C which is within the requirements of the production limitations.

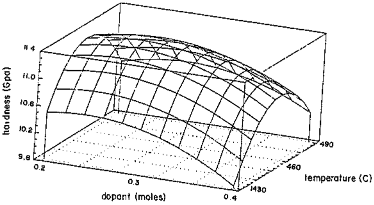

FIGURE 76: Plot of hardness versus dopant and temperature

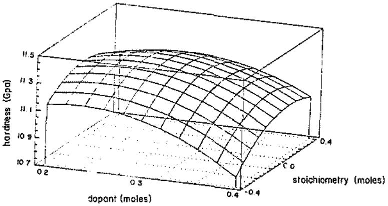

FIGURE 77: Plot of hardness versus dopant and stoichiometry

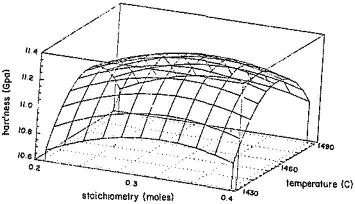

FIGURE 78: Plot of hardness versus stoichiometry and temperature

The regression result for strength data are listed in Table C.3, Appendix C.4. The data shows that only dopant and sintering temperature levels are important with their squared functions. The polynomial generated is:

$$\text{Strength} = 227{,}6 - 2{,}85C - 5{,}2A^2 - 10{,}8C^2 \qquad (31)$$

This is simpler than the previous expression for hardness and generates only one response surface as shown in Fig. 79. The regression analysis and residuals plots are shown in Appendix C.4, Figs C.5 - C.7. The data is shown to be normally distributed, as supported by the probability plot in C.8. This validates the use of the analysis of variance techniques used on this data.

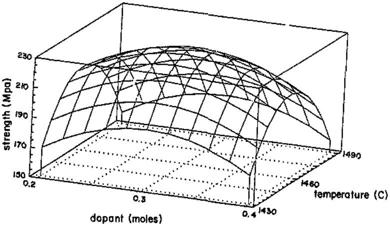

FIGURE 79: Plot of strength versus dopant and temperature

The hardness and strength data as analysed once again suggests a maximum has been reached for strength and hardness. The maximum hardness achieved was at the centre point and was 11,3 GPa. It is, however, known that zirconia-mullite of a hardness of 12,6 GPa was achieved for undoped material. It is possible that the second order design is too insensitive to pick up a second optimization path. This could happen as shown in Fig. 80, where the best optimization path runs through the design points.

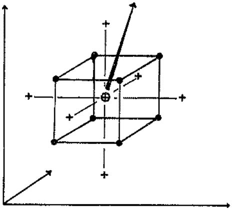

FIGURE 80: Hypothetical case where second order design may miss an optimization path

Another important aspect of this system is liquid phase exudation that occurs whenever substantial reaction occurs. The optimum hardness occurred at maximum density and Young's modulus representing a fully densified zircon-alumina with partial reaction as represented by the micrograph in Plate 4, Section 5.1.2. When reaction occurs the samples exude a liquid phase onto the surface with consequent reduction in properties. With these materials therefore the optimum hardness is achieved at the maximum density prior to reaction.

6.5 *REMOVAL OF LIQUID PHASE EXUDATION AT 1 490 C*

Stoichiometric samples were prepared with various quantities of dopant. These were fired at 1 490 C for 3 hours to determine the level at which liquid exudation ceases. The mixes were made in accordance with the stoichiometry of equation (22) Section 5.1.2 the molar ratios, densities and hardnesses are listed in Table 33.

TABLE 33: Density and hardness data for various compositions fired at 1 490 C for 3 hours

Composition	Dopant Addition (moles)	wt.%	Density (g/cm^3)	Hardness (GPa)
1	0,02	0,30	3,810	11,25
2	0,03	0,45	3,860	11,70
3	0,04	0,60	3,890	12,25
4	0,05	0,74	3,875	10,10
5	0,06	0,89	3,860	9,80
6	0,07	1,02	3,835	9,30

Compositions 1-3 showed no liquid exudation while compositions 4-6 did. A plot of composition and sintering temperature versus density is shown in Fig. 81. The shaded area shows the approximate area where liquid exudation occurs. Composition 3 borders this region, therefore from a safety point of view composition 2 is to be preferred. This is due to it being sufficiently dense yet avoiding the chance occurrence of liquid phases exuding due to uncontrolled furnace temperature variations.

An XRD trace (Fig. 82) of material of composition 2 fired for 3 hours at 1 490 C shows that reaction due to zirconia-mullite formation is approximately 50% complete. The degree of reaction appears to be related to the degree of densification achieved prior to reaction. This in turn is related to the degree of porosity removal or by the increase in reactant intergranular contact.

6.6 *COMPARATIVE EROSIVE WEAR EVALUATION*

Three sintered zircon-alumina materials were tested by comparative erosive wear tests by the method described in Section 4.2.2.5. These were compared against a 90% commercial alumina. The abrasive materials used were SiC grit with 110 µm average diameter and quartz sand with 150 µm average diameter. The angle of abrasion

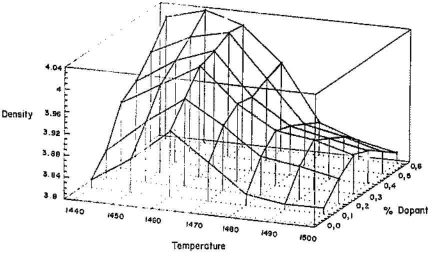

FIGURE 81: Plot of density versus sintering temperature and composition

used was 90°. Erosion was measured as mg of target material lost per kg of erodant used. The compositions of the samples tested are listed in Table 34. The compositions were stoichiometric zircon-alumina mixes based on the reaction chemistry of the dopants. The alumina was sintered at 1 490 C. The results are shown in Table 35.

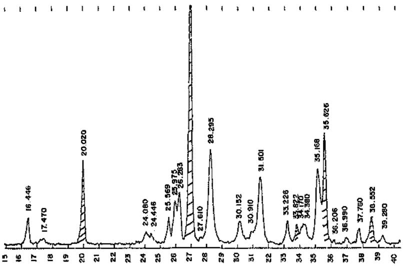

FIGURE 62: XRD trace of zircon-alumina with 0,02 moles SrO after sintering for 3 hours at 1 490 C

TABLE 34: Composition and sintering details

Composition	Dopant	Dopant (%)	Sintering Temperature (C)
1	SrO	0,45	1 490
2	SrO	3,7	1 460
3	ZnO	4,0	1 475

TABLE 35: Erosion results in mg loss per kg of erodent

Target Material	Wear (mg/kg of erodent)	
	SiC	Quartz
Composition 1	446	6
Composition 2	589	75
Composition 3	643	89
90% Alumina	600	74

The results show that composition 2, which was the centre point of the second, first order strategy (Section 6.4), had similar erosion properties to the alumina as tested. This fulfils the original requirements of the project. This material was only partially reacted as was the case for composition 1. Composition 1, however, showed a significant improvement in erosion properties being 25% more resistant to SiC and 12 times more resistant to quartz under the conditions used. This is probably due to the lower glassy *phase being present in composition 1. Composition 3, however,* showed poorer erosion properties compared to alumina despite being fully reacted to zirconia-mullite. A possible explanation is that weak grain boundaries are present.

A study of the effect of average particle size of starting materials was carried out to determine the effect on wear resistance of the final product. The results are presented in Fig. 83. The composition was varied with particle size by adding dopant in sufficient quantities to result in densification but at the same time avoiding liquid exudation. The sintering temperature was 1 490 C. The results show a steep increase in wear resistance as particle size decreases from 0,7 to 0,56 microns. Combined with the previous results this shows the importance of reduced dopant and particle size in achieving a wear resistant ceramic body in this system.

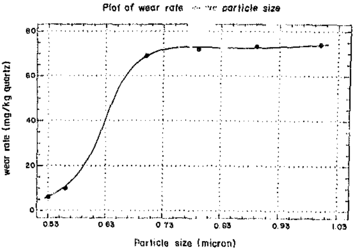

FIGURE 83: Plot of erosion versus raw material particle size of target material

7. DISCUSSION AND CONCLUSIONS

7.1 DISCUSSION

Reaction-sintered zircon-alumina has been studied with a range of novel dopants in order to develop a clearer understanding of the nature of the reactions. On the basis of these results one of the dopants, SrO, was selected for an optimization exercise. Through a number of iterations the material was improved on a range of properties, particularly hardness with respect to a commercial alumina material. Final comparative studies were carried out using particle impact erosion and showed reaction-sintered zircon-alumina to be comparable and in some instances superior to the alumina. In particular a zircon-alumina sintered at 1 460 C was shown to be equivalent to the alumina, and a zircon-alumina sintered at 1 490 C was shown to be vastly superior. The goals set at the beginning of this work have therefore been met. There are, however, some general comments to be made on the experimental design techniques used and some observations on reaction-sintered zircon-alumina.

The use of factorial designs has shown itself to be a useful tool in systematizing the study of multi-parameter effects on systems. However, it compliments rather than replaces conventional research techniques. In order to be efficiently used it is necessary to have a good understanding of the system under evaluation. It was twice shown during this study that whereas the mathematical analysis showed an optimum had been straddled by the experimental points, in fact potential optimization paths were not revealed by the statistical design alone. These paths were identified by a knowledge of the system built on empirical experimentation during the preliminary studies. The use of these techniques in general, however, is a safer and more economical way of approaching complex problems. The safety factor is that more meaningful experimental conditions can be covered, thus minimizing the chance of missing an important factor.

Reaction-sintered zircon-alumina is a complex system. Depending on the setting of experimental parameters products with potentially good properties can, for a slight shift in parameter values, give mediocre or poor properties. This point was emphasized by Boch and Giry [79] who stated that the main drawback to reaction-sintering was sensitivity to powder characteristics, which makes it difficult to control. As a result of this observation they doubted whether zirconia-mullite was commercially viable. The results of this investigation indicate that as long as the source of variation is known and monitored other parameters may be manipulated to maintain the desired quality within defined limits. In order to define these limits and respond efficiently to variation the processing parameters should ideally be numerically defined as shown in developing response surfaces.

Although further study is required some tentative comments can be made on the effect of microstructure on the properties of sintered zircon-alumina for the Group II A doped materials. The properties of hardness, strength and wear resistance reached an optimum in this material with a combination of high density and limited degree of reaction. This contrasts somewhat with Ni^{2+} and Zn^{2+} materials which achieved optimum properties with full reaction. Another important difference was the high degree of densification achieved for the Group II A doped materials prior to full reaction as opposed to the lesser degree of densification for the Ni^{2+} and Zn^{2+} doped materials.

There are considerable dangers in making general statements on microstructural effects on properties of zirconia-mullite *per se* owing to the complexity of competing physico-chemical processes in conjunction with competing toughening mechanisms. For this reason only the SrO-doped material will be considered as information on the other systems is incomplete.

A number of aspects are involved during the sintering process which have differing effects on the properties. The first is the process of densification which is a *sine qua non* for structural ceramic processing and requires little further comment. In the SrO-doped system the densification of reactants prior to full reaction is particularly pronounced. Densification is usually accompanied by grain growth which is generally deleterious to mechanical properties, part of which may be attributed to a lowering of the internal surface energy with reduced grain boundary area. Associated with this is an increase in width of intergranular boundaries occurring with reduced internal surface area. This is a result of the distribution of a fixed volume of impurity or dopant phases over reduced areas. Since many of these grain boundary phases are either amorphous or less robust than the grains this phenomenon increases the probability of crack initiation occurring for a particular event.

The zircon-alumina to zirconia-mullite reaction occurs by a solution-diffusion-precipitation process similar to that described in Fig. 15 [32]. Being essentially a recrystallization process, impurities which existed in the zircon will be concentrated in the intergranular boundary phases, ultimately increasing the volume of these phases. This would combine with the grain growth effect to the detriment of the properties.

Associated with the reaction is a volume increase which must result in major changes in internal stresses. With the related increase in more grain boundary mobility, stress relaxation could occur. Alternatively microcracking at the grain boundaries may be the mechanism of stress relaxation. Microcracking appears to be an im[illegible]cant toughening mechanism in zirconia-mullite as suggested from the literature [42,60]. However, although microcracking can provide toughening to the bulk of the material, it is more likely to be deleterious at a microstructural level where erosion by particle impact is operative since the initiation sites for crack growth have already been provided. The energy of impacting, abrasive, angular particles is generally transmitted at a concentrated point. This results either in grain chipping or crack growth along grain boundaries resulting in grains falling out. The latter mechanism is likely to be assisted by pre-existing microcracks. This may explain the poor performance of Zn^{2+} doped zirconia-mullite to abrasive wear reported in Table 35.

Finally, in the SrO-doped system reaction is accompanied by the appearance of a permanent liquid phase which is dependent on the concentration and dopants and can reach excessive proportions. This results in a deterioration in properties. In summary, it appears that any advantage in achieving full reaction to zirconia-mullite in these systems is more than outweighed by the disadvantages. The best material achieved is a partially reacted fine-grained, dense body with minimal intergranular phases.

The question remains as to the nature of toughening mechanisms in such a body. Although transformation toughening has been shown to be effective in an undoped zirconia-mullite [58] this is likely to be a small contribution in a partially reacted body where tetragonal zirconia may make up as little as 4% of the total volume. Such a body, which contains four major phases, is likely to have a high degree of internal stresses due to thermal mismatch. It is probable that this results in toughening due to crack bowing and deflection mechanisms. These have been specifically mentioned as possible mechanisms in the literature for mullites containing embedded alumina and zirconia particles [16,43]. Orange *et al.* [16] concluded that published toughening mechanisms cannot explain, by themselves, the mechanical properties of the composites they studied. Rather a combination of different mechanisms is operative each of them being more or less effective according to composition and microstructure. These conclusions are equally valid for the SrO-doped zircon-alumina-zirconia-mullites described in this study. The main difference between the current work and that reported in the literature is the use of finer particle size and partial reaction to achieve the best results with a novel dopant.

It has been demonstrated that the processing of a commercially viable reaction-sintered zircon-alumina is possible. This can be done by a pragmatic quantification of processing parameters in relation to properties within the restrictions applied by basic commercial realities. It has further been demonstrated that substantial improvements in properties are possible which suggests that these materials may have wider applications than originally envisaged.

7.2 CONCLUSIONS

Some general conclusions can be made on both experimental design techniques and on the nature of zircon-alumina ceramics studied in this work.

- Factorial designed experimentation has been shown to be a powerful research tool when used in conjunction with conventional procedures. The main benefit is through provision of a wider net in covering potentially important parameters in a labour efficient manner.
- Multifactor optimization techniques are not infallible when used in the absence of critical evaluation of the meaning of the results. Important optimization routes can be missed which would only be picked up by a good knowledge of the system.
- CaO, SrO and BaO show themselves to be efficient dopants in the zircon-alumina system in assisting densification. Owing to liquid phase exudation occurring with full reaction, the best properties were achieved with partial reaction when using these dopants.
- NiO and ZnO-doped zircon-alumina exhibit best properties with full reaction but fail to densify fully, under similar processing conditions as used for the group II A dopants.
- A double-doped system of SrO and ZnO showed a 50 C reduction in reaction temperature over the single-doped systems.
- Particle size of zircon and alumina prior to sintering has a major effect on wear resistance of partially reacted SrO-doped zircon-alumina. Particle sizes of 0,5 µm produce ceramics 10 times more resistant to quartz erosion than particle sizes of 0,7 µm.

- In partially reacted zircon-alumina-zirconia-mullite ceramics which have been *found to be particularly* wear resistant, a combination of toughening mechanisms are probably active. It seems probable that crack bowing and *deflection toughening* mechanisms would be more important than microcracking and transformation toughening.

7.3 *SUGGESTIONS FOR FURTHER WORK*

The range of dopants studied and *potential interactions of dopants* in conjunction with material characterization pose an almost endless prospect for further study. As a result only the key possibilities can be listed:

1) TEM analysis of microstructure, especially analysing the nature of grain boundaries in conjunction with erosive wear evaluation.
2) Definition of fully optimized zircon-alumina by dopant reduction towards an undoped material.
3) Quantification of the effect on properties of annealing of high-dopant materials.
4) Establish a lower optimization temperature using a double dopant system such as SrO/ZnO.

8. *LITERATURE*

1. N Claussen, J Steeb and R F Pabst, Effect of induced microcracking on the fracture *toughness of ceramics*, *Ceram.* Bull., 56, (1977), 599-562.

2. F F Lange, Transformation toughening, Part 4, fabrication, fracture toughness and strength of Al_2O_3-ZrO_2 composites. J. *Mat. Sci.*, 17, *(1982)*, 247-254.

3. *N Claussen*, *Strengthening* strategies for ZrO_2-toughened ceramics at high temperatures, Mat. Sci. Eng., 71, (1985), 23-38.

4. T Kosmac, M V Swain and N Claussen, The role of tetragonal and monoclinic ZrO_2 particles in the fracture *toughness of* Al_2O_3-ZrO_2 composites, Mat. Sci. Eng., 71, (1985), 57-64.

5. R C Garvie, Microstructure and performance of an alumina-zirconia tool bit, J. Mat. Sci. Lett., 3, (1984), 315-318.

6. E P Butler, Critical assessment. Transformation-toughened zirconia ceramics, Mat. *Sci. Tech.*, 1, *(1985)*, 417-432.

7. E Di Rupo, T G Carrathurs *and R J Brook*, *Identification* of stages in reactive hot-pressing, J. Am. Ceram. Soc., 61, (1978), 468-469.

8. E Di Rupo, E Gilbart, T G Carruthers and R J Brook, Reaction *hot-pressing of zircon-alumina* mixtures, J. Mat. Sci., 14, (1979), 705-711.

9. E Di Rupo, M R Anseau and R J Brook, Reaction sintering: correlation between densification and reaction, J. *Mat. Sci.*, 14, (1979), 2924-2928.

10. E Di Rupo and M R Anseau, Solid state reaction in the $ZrO_2.SiO_2$-αAl_2O_3 system, J. Mat. Sci., 15, (1980), 114-118.

11. P D D Rodrigo and P Boch, High purity mullite ceramics by reaction sintering, Int. J. High Tech. Ceram., 1, (1985), 3-30.

12. J S Moya and M I Osendi, Microstructure and mechanical properties of mullite/ZrO_2 composites, J. Mat. Sci., 19, (1984), 2909-2914.

13. K S Mazdiysni and L M Brown, Synthesis and mechanical properties of stoichiometric aluminium silicate (mullite), J. Am. Ceram. Soc., 55, (1972), 548-552.

14. N Claussen and J Jahn, Mechanical properties of sintered, in situ-reacted mullite-zirconia composites, J. Am. Ceram. Soc., 63, (1980), 228-229.

15. A I Kingon, N A Stone and N S Carr, Performance of some zirconia-based ceramics under conditions of particle impact erosion, High Tech. Ceramics, Elsevier Science publ., B.V., Amsterdam, (1987), 2657-2666.

16. G Orange, G Fantozzi, F Cambier, C Leblud, M R Anseau and A Leriche, High temperature mechanical properties of reaction sintered mullite/zirconia and mullite/alumina/zirconia composites, J. Mat. Sci., 20, (1985), 2533-2540.

17. B H Mussler and M W Shafer, Preparation and properties of mullite-cordierite composites, Ceram. Bull., 63, (1984), 705-710.

18. J H Chesters, Refractories: Production and Properties, London, The Iron and Steel Institute, (1973), 271-273.

19. M G M U Ismail, Z Nakai and K Minegishi, Synthesis of Mullite Powder and its Characteristics, Int. J. High Tech. Ceram., 2, (1986), 123-134.

20. R C Garvie, R H Hanikk and R T Pascal, Ceramic Steel, Nature, 258, (1975), 703.

21. P Pena and S de Aza, The zircon thermal behaviour: effect of impurities, Part 1, J. Mat. Sci., 19, (1984), 135-142.

22. P Pena, F Guitian and S de Aza, The zircon thermal behaviour: effect of impurities, Part 2, J. Mat. Sci., 19, (1984), 143-149.

23. N L Bowen and J W Greig, The system Al_2O_3-SiO_2, J. Am. Ceram. Soc., 7, (1924), 242.

24. S Aramaki and R Roy, Revised phase diagram for the system Al_2O_3-SiO_2, J. Am. Ceram. Soc., 45, (1962), 229-242.

25. I A Aksay and J A Pask, Stable and metastable equilibria in the system SiO_2-Al_2O_3, J. Am. Ceram. Soc., 58, (1975), 507-512.

26. R F Davis and J A Pask, Diffusion and reaction studies in the system Al_2O_3-SiO_2, J. Am. Ceram. Soc., 55, (1972), 525-531.

27. J S Moya and M I Osendi, Effect of ZrO_2 (ss) in mullite on the sintering and mechanical properties of mullite/zirconia composites, J. Mat. Sci. Lett., 2, (1983), 599-601.

28. T R Dinger, K M Krishnan, G Thomas, M I Osendi and J S Moya, Investigation of ZrO_2/mullite solid solution by energy dispersive X-ray spectroscopy and electron diffraction, Acta Metall., 10, (1984), 1601-1607.

29. P Pena, P Miranzo, J S Moya and S De Aza, Multicomponent toughened ceramic materials obtained by reaction sintering, Part 1, ZrO_2-Al_2O_3-SiO_2-CaO system, J. Mat. Sci., 20, (1985), 2011-2022.

30. P Miranzo, P Pena, J S Moya and S De Aza, Multicomponent toughened ceramic materials obtained by reaction sintering, Part 2, system ZrO_2-Al_2O_3-SiO_2-MgO, J. Mat. Sci., 20, (1985), 2702-2710.

31. M F Melo, J S Moya, P Pena and S De Aza, Multicomponent toughened ceramic materials obtained by reaction sintering, Part 3, system ZrO_2-Al_2O_3-SiO_2-TiO_2, J. Mat. Sci., 20, (1985), 2711-2788.

32. J Rincon, G Thomas, P Pena, S de Aza and J S Moya, Reaction sintered zirconia-mullite composites with CaO, Journal de Physique, 47, (1986), C1-423-427.

33. P Miranzo, M I Osendi and J S Moya, Influence of processing method on microstructural and mechanical properties of mullite /ZrO_2 composites, Journal de Physique, 47, (1986) C1-417-421.

34. R L Coble, A model for boundary diffusion controlled creep in polycrystalline materials, J. Appl. Phys., 34, (1963), 1679-82.

35. R L Coble, diffusion models for hot pressing with surface energy and pressure effects as driving forces, J. Appl. Phys., 41, (1970), 4798-4807.

36. M R Anseau, E Di Rupo, C Leblud, F Cambier and P Fierens, Le frittage réactif à l'ètat solide de poudres cèramiques, Silicates Industriels, 46, (1981), 17-27.

37. H M M Diz and J M Ferreira, Study of the factors influencing the slip-casting of mullite-zirconia ceramics, Br. Ceram. Proc., 37, (1986), 159-165.

38. P Pilate and F Cambier, Synthesis and reaction sintering with alumina of plasma sprayed zircon powder, Silicates Industriels, 51, (1986), 95-98.

39. P Boch, G Kapelski and J P Giry, Sintering properties of dissociated and reassociated zircon, Br. Ceram. Proc., 37, (1986), 149-160.

40. Y Masahiro, K Masafumi and S Shigeyuki, Crystallization of mullite-zirconia amorphous materials prepared by Rapid Quenching, Yogyo Kyokai Shi, 95, (1987), 202-208.

41. P F Becker and T N Tiegs, Silicon carbide whisker-zirconia reinforced mullite and alumina ceramics, US Patent No. 4,657,877, 14 April 1987.

42. P Miranzo, P Pena, S De Aza, J S Moya, J Ma Rincon and G Thomas, TEM study of reaction-sintered zirconia-mullite composites with CaO and MgO additions, J. Mat. Sci., 22, (1987), 2987-2992.

43. C Baudin, F Cambier and L Delaey, Fractographic and acoustic emission of mullite-alumina-zirconia composites prepared by reaction sintering, J. Mat. Sci., 22, (1987), 4398-4402.

44. J Ma Rincon, P Fernández and J Llopis, Characterization of zirconia/mullite ceramics by cathodoluminescence technique, Appl. Phys., A44, (1987) 299-303.

45. K Tsukuma, K Ueda and M Shimada, Strength and fracture toughness of isostatically hot-pressed composites of Al_2O_3 and Y_2O_3-partially stabilized ZrO_2, J. Am. Ceram. Soc., 68, (1985), C4-C5.

46. M V Swain and N Claussen, Comparison of K_{IC} values for Al_2O_3-ZrO_2 composites obtained from notched-beam and identation strength techniques, J. Am. Ceram. Soc., 66, (1983), C-27-C-29.

47. A W Paterson and R Stevens, Comparison of identation and notched bar toughness of TZP ceramics: Relevance to models of fracture process, J. High. Tech. Ceram., 2, (1986), 221-230.

48. F F Lange, Transformation toughening Part 1, size effects associated with the thermodynamics of constrained transformations, J. Mat. Sci., 17, (1982), 225-234.

49. R C Garvie and M V Swain, Thermodynamics of the tetragonal to monoclinic phase transformation in constrained zirconia microcrystals, Part 1, J. Mat. Sci., 20, (1985), 1193-1200.

50. R C Garvie, Thermodynamic analysis of the tetragonal to monoclinic transformation in a constrained zirconia microcrystal, Part 2, J. Mat. Sci., 20, (1985), 3479-3486.

51. R W Davidge, Mechanical behaviour of ceramics. Cambridge Solid State Series, Cambridge Univ. Press, 1980.

52. A G Evans and R M Cannon, Toughening of brittle solids by martensitic transformations, Acta Metall., 34, (1986), 761-800.

53. P F Becher, M V Swain and M K Ferber, Relation of transformation temperature to the fracture toughness of transformation-toughened ceramics, J. Mat. Sci., 22, (1987), 76-84.

54. D J Green, Critical microstructures for microcracking in Al_2O_3-ZrO_2 composites, J. Am. Ceram. Soc., 65, (1982), 610-614.

55. H Ruf and A G Evans, Toughening by monoclinic zirconia, J. Am. Ceram. Soc., 66, (1983), 328-332.

56. E Bischoff and M Rühle, Twin boundaries in monoclinic ZrO_2 particles confined in a mullite matrix, J. Am. Ceram. Soc., 66, (1983), 123-127.

57. F F Lange, The interaction of a crack front with a second-phase dispersion, Philos. Mag., 179, (1970), 983-992.

58. J S Wallace, G Petzow and N Claussen, Microstructure and property development of in situ-reacted-ZrO_2 composites, advances in ceramics, Vol. 12, science and technology of zirconia 2, The Am. Ceram. Soc. Inc., 1984, 436-441.

59. M I Osendi, P Miranzo and J S Moya, Solid-solution effects on the fracture toughness of mullite - ZrO_2 composites, J. Mat. Sci. Lett., 4, (1985), 1026-1028.

60. V P Dravid, M R Notis and C E Lyman, Twinning and microcracking associated with monoclinic zirconia in the eutectic system zirconia-mullite, *J. Am. Ceram. Soc.*, 71, (1988), C219-C221.

61. B Joliet, F Cambier, L Dapra, C Leblud and A Leriche, Microstructural and mechanical characterization of mullite-zirconia composites containing yttria, *Journal de Physique*, 47, (1986), C1-723-728.

62. A Leriche, F Cambier and R J Brook, Study of some factors influencing the microstructural development of mullite-zirconia composites obtained by reaction sintering, Br. Ceram. Proc., 37, (1986), 167-177.

63. J S Moya, P Miranzo, P Pena and S de Aza, Processing parameters in reaction sintered ceramics, Soc. Esp. Cerâm. Vidr., (1986), 122-133.

64. D C Montgomery, Design and analysis of experiments, John Wiley & Sons publ., (1984).

65. R E Walpole and R H Myers, Probability and Statistics for Engineers and Scientists, Collier Macmillan publ., 1978.

66. R Caulcutt, Statistics in Research and Development, Chapman and Hall publ., 1983.

67. W G Cochran and G M Cox, Experimental Designs, John Wiley & Sons publ., 1957.

68. C Chatfield, Statistics for Technology - a course in applied statistics, Chapman and Hall publ., 1983.

69. G E P Box, W G Hunter and J S Hunter, Statistics for Experiments - an introduction to design, data analysis and model building, John Wiley & Sons publ., 1978.

70. R A Fisher, Design of Experiments, Oliver & Boyd publ., 1951.

71. G Z Yin and D W Jillie, Orthogonal design for process optimization and its applications in plasma etching, Solid State Technology Mag., (1987) 127-132.

72. J S Hunter, The inverse Yates algorithm, Technometrics, 8, (1966), 177-183.

73. G R Anstis, P Chantikul, B R Lawn and D B Marshall, A critical evaluation of identation techniques for measuring fracture toughness; I direct crack measurements, J. Am. Ceram. Soc., 64, (1981), 533-543.

74. E Papadakis, Ultrasonic velocity and attenuation, Physical Acoustics, 12, (1976), 277.

75. J Levitt, The high temperature and pressure ultrasonic system (the solid cell), Internal Report for NIMR - CSIR, Pretoria (1986) IMAT 112.

76. J E Huhey, Inorganic Chemistry - Principles of Structure and Reactivity, Harper & Row publ., (1975) 74-75.

77. A G Evans, M E Gulden and M Rosenblatt, Impact damage in brittle materials in the elastic-plastic response régime, Proc. Roy. Soc., A361, (1978), 343-365.

78. S M Wiederhorn and B R Lawn, Strength degradation of glass impacted with sharp particles: I. Annealed surfaces, J. Am. Ceram. Soc., 62, (1979), 66-70.

79. P Boch and J P Giry, Preparation and properties of reaction-sintered mullite-ZrO_2 ceramics, Mat. Sci. Eng., 71, (1985), 39-48.

APPENDIX A

BASIC PRINCIPLES OF ORTHOGONAL DESIGN AND OPTIMIZATION

A.1 *Some Problems with Classical Experiments* (adapted from *Box et al.* [69] Chapter 15)

Classical research, in determining the effect of variables on a measured parameter, is based on the one-parameter-at-a-time (OPAAT) method. This method, in which experimental factors are varied one at a time, with the remaining factors held constant, is widely used to conduct research. This approach provides an estimate of the effect of a single variable at a selected fixed point in a multivariable space. However, for such an estimate to have any general relevance, it is necessary to assume that the effect would be the same at any other point in the multivariable space. In reality, this is rarely the case, as can be appreciated by considering Fig. A.1. The situation represented shows the weakness of the OPAAT approach by illustrating two facets of a hypothetical sintering scheme for a ceramic. Dependent on the selection of the time variable completely different information is received on the effect of temperature.

Another problem typically associated with the OPAAT approach can be demonstrated by attempting to optimize on the system just described. An attempt to maximize the strength of the ceramic with respect to time and temperature might follow the course illustrated. If the temperature is fixed at T = 1 225 C and sintering time was varied from 60 to 180 minutes the results on strength would resemble that shown in Fig. A.2a. This would lead to the conclusion that the best sintering time was 130 minutes for this fixed temperature.

Following OPAAT strategy, 130 minutes would be chosen as the "best" fixed value and temperature would be varied. This could

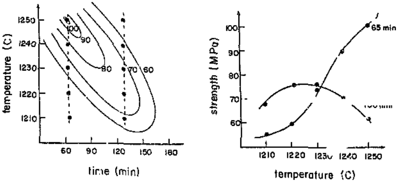

FIGURE A.1: Hypothetical response surface representing strength versus sintering time and temperature, with points *for one-variable-at-a-time approach*

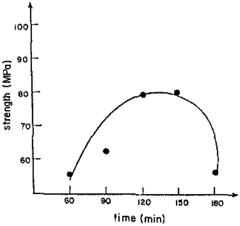

(a) First set of experiments: yield versus reaction time, temperature held fixed at 1 225 C

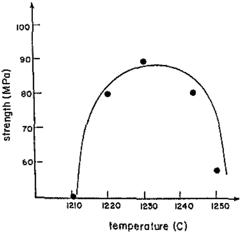

(b) Second set of experiments: yield versus temperature, reaction time held fixed at 130 minutes

FIGURE A.2: Hypothetical results from the OPAAT approach give a graph similar to that shown in Fig. A.2b. The maximum strength *obtained is at a temperature of 1 225 C. The conclusion* now seems justified that the overall maximum strength of 85 MPa is achieved by sintering for 130 minutes at 1 225 C. In the hypothetical example chosen this would be erroneous as can be appreciated by considering Fig. A.3. The real maximum strength is approximately 105 MPa at sintering time of 65 minutes and 1 255 C. The failure in this case of OPAAT strategy to correctly optimize strength is that the approach tacitly assumes that the maximizing value of one parameter is independent of the level of the other. In most systems this is not true.

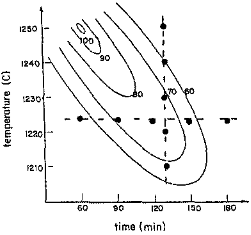

FIGURE A.3: Possible true response surface representing strength versus sintering time and temperature with points shown per OPAAT approach

A.2 *An Example of a Simple Factorial Experiment*

In a 2^2 design each parameter under investigation is coded initially at two levels. The high level is represented by '+' and the low level by '-'. There are two parameters of interest in this case, namely temperature and time. The plus and minus sign *are short-hand notation* for +1 and -1 respectively and can be multiplied as such to provide parameter interactions. The design of the experiment contains every possible combination of high and low settings and is usually represented in standard Yates order as shown in *Table A.1*.

TABLE A.1: Standard Yates order for a 2^2 factorial design

Number	Observation	Parameters A	Parameters B	Interactions AB
1	+	-	-	+
2	+	+	-	-
3	+	-	+	-
4	+	+	+	+

Assuming the levels of temperature and time chosen for the experiment were 1 220 and 1 230 C, and 120 and 150 minutes respectively the points would be represented as shown in Fig. A.4. If for example, the strengths of each experimental setting were found to be *62, 76, 72 and 75 MPa respectively, a first order polynomial* can be calculated as described in Table A.2. The measured strength for each experimental setting is written in across all the columns in the design and takes on the sign of each position as shown. Each column is then summed and divided by the appropriate divisor to provide the relevant coefficient. The first degree polynomial is taken from the coefficients as shown by the equation

$$\text{STRENGTH} = 71{,}75 + \frac{3{,}5}{2} A - \frac{2{,}5}{2} B - \frac{4{,}5}{2} AB \text{ (MPa)} \qquad \text{A.1}$$

where A and B are the temperature and time codes respectively.

Equation A.1 summarizes to a first approximation the situation as affected by the chosen parameters. In this case an increase in the sintering temperature has a positive effect on strength whereas an increase in sintering time has a negative effect. A

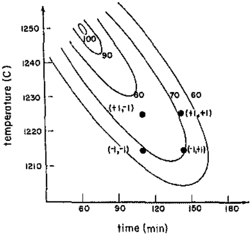

FIGURE A.4: Representation of hypothetical case for a 2^2 factorial experiment with *factor codes*

TABLE A.2: Calculation of results for hypothetical 2^2 factorial

Number	Observation	Parameters A	 B	Interactions AB
1	+ 69	- 69	- 69	+ 69
2	+ 77	+ 77	- 77	- 77
3	+ 71	- 71	+ 71	- 71
4	+ 70	+ 70	+ 70	+ 70
Divisor	4	2	2	2
Coefficient	71,75	+ 3,5	- 2,5	- 4.5

positive increase in the interaction (i.e. increasing or decreasing both temperature and time simultaneously) has a negative effect on strength. *In order, therefore, to achieve the maximum strength* within the set parameter levels in this case one should select the high temperature setting with the low time setting. This is described by Yates experiment No. 2 in Table A.1. Substituting the level codes into A, B and AB in equation *A.1 yields a strength* of 77 MPa. For optimization it is assumed that further increases in temperature and decreases in sintering time should improve the strength. This is discussed in Appendix A.4.

A.3 *Interaction and Curvature Check*

The interactions, if present, are indicative of a certain degree *of curvature. The interaction effect* is calculated for the example just described in exactly the same way as for the parameters as shown in Table A.2. In this case the interaction coefficient is -4,5 MPa. The meaning of this can be seen by referring to Fig. A.5a-c.

Figure A.5a represents the simple effect of the two parameters with no interactions. The effects are additive and so gives a *planar response surface.* Figure A.5b shows the effect of the negative interaction giving a "minimax" response surface where the centre is a col between two hills. This can be compared to a positive interaction of the same magnitude described by Fig. A.5c.

The curvature is a measure of the discrepancy between the average of the results for the four coded settings and the centre point which has the coding (0,0). It is marked as run number 0 in Fig. A.5. *The mathematical meaning of variance* between the centre point strength value is described by the coefficients of the squared terms in a second degree polynomial. A second degree polynomial takes the form

$$Z = \beta_0 + \beta_1 A + \beta_2 B + \beta_{11} A^2 + \beta_{11} B^2 + \beta_{22} B^3 + \beta_{12} AB \qquad A.2$$

where β_0 represents the average of the coded points, β_1 and β_2 the effects of the parameters, $(\beta_{11} + \beta_{22})$ the variance between the centre point and the average, and β_{12} the interaction effect. A A and B are the coded parameter values. For a full estimation of

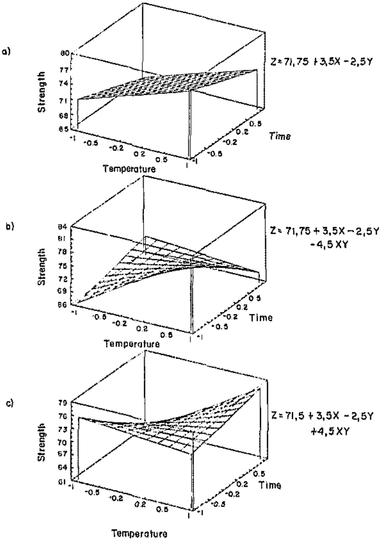

FIGURE A.5: Plot of strength versus temperature and time for hypothetical example showing effect of parameter interactions .

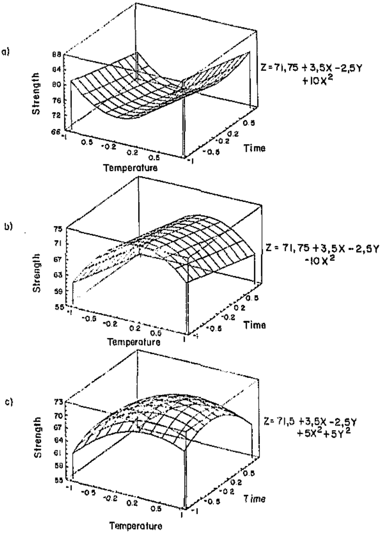

FIGURE A.6: Plot of strength versus temperature and time for hypothetical example showing effect of central curvature

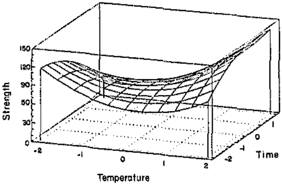

FIGURE A.7: Plot of strength versus temperature and time for a hypothetical situation described by the polynomial in equation A 3

$$Z = 71{,}75 + 10X - 5Y + 10X^2 - 5Y^2 + 8{,}5XY \qquad A.3$$

all the coefficients, higher order experimental designs and least squares regression are required. These are briefly discussed in Appendices A.7 and A.8.

The topoghraphical effects of the degree of curvature is illustrated in Fig. A.6a-c. Figure A.6a and b shows the effect of a positive and negative deviation from centrality as described by one squared parameter. Figure A.6c shows the effect of two positive squared terms. *A typical response surface of a full second* order polynomial is illustrated in Fig. A.7 showing the potential complexity that can be employed.

A.4 *The Path of Steepest Ascent*

The path of steepest ascent is calculated from the first order polynomial A.1. Starting at the centre of the experimental region where the coded value of A and B are both zero, the path is followed by moving 3,4 units along the A axis for every -2,5 units along the B axis. This is illustrated by the dotted line in Fig. A.8. The length of the steps can be varied in size. A convenient *set of points on the path* of steepest ascent are also shown in Fig. A.8 and Table A.3. This path is followed until a maximum has been found and then a second first order design is planned close to the maximum. The exercise is repeated until the centre point gives a *strength figure that is larger than the other coded points.*

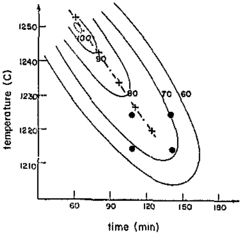

FIGURE A.8: Path of steepest ascent with convenient set points

TABLE A.3: Points on the path of steepest ascent, hypothetical example

	Coded Conditions		Temperature (C)	Time (mins)	Run Number	Observed Strength
	A	B				
Centre conditions	0	0	1 225	135	0	71,75
Path of steepest ascent	1,4	-1	1 230	120	1	78,0
	2,8	-2	1 239	105	2	83,0
	4,2	-3	1 246	90	3	90,0
	5,6	-4	1 253	75	4	*100,0*
	7,0	-5	1 260	60	5	80,0

This implies that the other points straddle a maximum, at which point a second order design is employed which will be described later.

A.5 *First Order Factorial Designs*

Table A.4 summarizes the design matrices for 2^2, 2^3 and 2^4 factorial experiments, for 2, 3 and 4 factors respectively. This results in 4, 8 and 16 experimental settings, and shows the pattern of factorial designs. The larger the design the more complex the nature of the interactions. In general the large interactions such as ABCD tend to zero as one of the parameters is likely to be acting against the trend of the others. The result is potentially redundant information. It is possible to reduce the size of the higher order factorials such as 2^6 which requires 64 experimental settings to a half or a quarter of the original size. If this is carefully done the effects of the parameters and most of the important interactions can still be analysed. This is discussed in most texts on factorial designs [67-70].

TABLE A.4: Design matrices for 2^2, 2^3 and 2^4 factorial experiments

A	B	AB	C	AC	BC	ABC	D	AD	BD	ABD	CD	ACD	BCD	ABCD
-	-	+	-	+	+	-	-	+	+	-	+	-	-	+
+	-	-	-	-	+	+	-	-	+	+	+	+	-	-
-	+	-	-	+	-	+	-	+	-	+	+	-	+	-
+	+	+	-	-	-	-	-	-	-	-	+	+	+	+
-	-	+	+	-	-	+	-	+	+	-	-	+	+	-
+	-	-	+	+	-	-	-	-	+	+	-	-	+	+
-	+	-	+	-	+	-	-	+	-	+	-	+	-	+
+	+	+	+	+	+	+	-	-	-	-	-	-	-	-
-	-	+	-	+	+	-	+	-	-	+	-	+	+	-
+	-	-	-	-	+	+	+	+	-	-	-	-	+	+
-	+	-	-	+	-	+	+	-	+	-	-	+	-	+
+	+	+	-	-	-	-	+	+	+	+	-	-	-	-
-	-	+	+	-	-	+	+	-	-	+	+	-	-	+
+	-	-	+	+	-	-	+	+	-	-	+	+	-	-
-	+	-	+	-	+	-	+	-	+	-	+	-	+	-
+	+	+	+	+	+	+	+	+	+	+	+	+	+	+

A.6 *Analysis of Factorials Using Normal Probability Plots*

The problem of determining whether a measured effect is due to experimental error or is real can be analysed using normal probability plots. This technique is generally only useful for factorial designs of *4 factors or more.*

A normal distribution is *shown in Fig. A.9a* for a set of data presented by the black points. If these points are ranked from lowest to highest the probability of their appearance can be approximated by the equation,

$$\frac{100\ (i-½)}{m} \qquad \text{A.4}$$

for $i = 1,2,\ldots,m$.

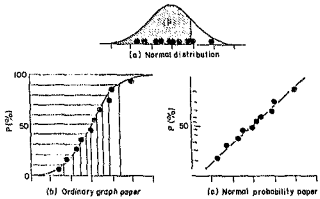

FIGURE A.9: Normal probability plots

If the data is normally distributed and the probability of each point is plotted against its value the graph will be sigmoidal as shown in Fig. A.9b. When the same points are plotted on normal probability paper they fall on a straight line as shown in Fig. A.9c. The use of this analysing real effects in a 2^4 factorial experiment can be demonstrated by considering Fig. A.10. All the effects due to experimental error will tend to follow a normal *distribution and fall on* a straight line as shown. Any points falling off the line cannot be explained as normal variance and has to be a real effect. In this case all four parameters and one interaction *are real while the remainder can be* considered as being due to experimental error.

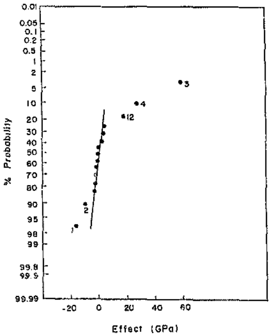

FIGURE A.10: Plot of probability versus Young's modulus effects

If the data is normally distributed and the probability of each point is plotted against its value the graph will be sigmoidal as shown in Fig. A.9b. When the same points are plotted on normal probability paper they fall on a straight line as shown in Fig. A.9c. The use of this analysing real effects in a 2^4 factorial experiment can be demonstrated by considering Fig. A.10. All the effects due to experimental error will tend to follow a normal distribution and fall on a straight line as shown. Any points falling off the line cannot be explained as normal variance and has to be a real effect. In this case all four parameters and one interaction are real while the remainder can be considered as being due to experimental error.

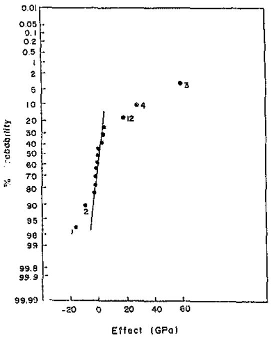

FIGURE A.10: Plot of probability versus Young's modulus effects

A.7 *Second Order Factorial Designs*

In order to estimate regression coefficients for a second degree polynomial each variable must have at least three different levels. Some of the most effective designs of this nature are *central composite rotatable designs.* The matrix for two and three parameters are given in Tables A.5 and A.6 respectively. The geometry of these designs are shown in Figs A.11 and A.12 respectively.

TABLE A.5: Central composite rotatable design *for two parameters*

Average	A	B	A^2	B^2	AB
1	-1	-1	1	1	1
1	1	-1	1	1	-1
1	-1	1	1	1	-1
1	1	1	1	1	1
1	-1,414	0	2	0	0
1	1,414	0	2	0	0
1	0	-1,414	0	2	0
1	0	1,414	0	2	0
1	0	0	0	0	0
1	0	0	0	0	0
1	0	0	0	0	0
1	0	0	0	0	0
1	0	0	0	0	0

TABLE A.6: Central composite rotatable design for three parameters

Average	A	B	C	A^2	B^2	C^2	AB	AC	BC	ABC
1	-1	-1	-1	1	1	1	1	1	1	-1
1	1	-1	-1	1	1	1	-1	-1	1	1
1	-1	1	-1	1	1	1	-1	1	-1	1
1	1	1	-1	1	1	1	1	-1	-1	-1
1	-1	-1	1	1	1	1	1	-1	-1	1
1	1	-1	1	1	1	1	-1	1	-1	-1
1	-1	1	1	1	1	1	-1	-1	1	-1
1	1	1	1	1	1	1	1	1	1	1
1	-1,682	0	0	2,828	0	0	0	0	0	0
1	1,682	0	0	2,828	0	0	0	0	0	0
1	0	-1,682	0	0	2,828	0	0	0	0	0
1	0	1,682	0	0	2,828	0	0	0	0	0
1	0	0	-1,682	0	0	2,828	0	0	0	0
1	0	0	1,682	0	0	2,828	0	0	0	0
1	0	0	0	0	0	0	0	0	0	0
1	0	0	0	0	0	0	0	0	0	0
1	0	0	0	0	0	0	0	0	0	0
1	0	0	0	0	0	0	0	0	0	0
1	0	0	0	0	0	0	0	0	0	0
1	0	0	0	0	0	0	0	0	0	0

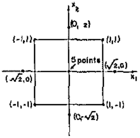

FIGURE A.11: Central composite design for two parameters

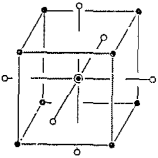

FIGURE A.12: Central composite design for three variables

A.8 *Analysis of Variance of Replicated Designs*

If the measurement for each point is replicated the use of the powerful analysis of variance technique, based on the fixed effects linear statistical model can be employed. For a two-*parameter factorial design* the results can be described by the linear statistical model

$$y_{ijk} = \mu + \tau_i + \beta_j + (\tau\beta)_{ij} + \epsilon_{ijk} \qquad \text{A.5}$$

where $i = 1, 2, \ldots, a$
$j = 1, 2, \ldots, b$
$k = 1, 2, \ldots, n$

and μ is the overall mean effect, τ_i is the effect of the i-th level of the row parameter A, β_j is the effect of the j-th level of column parameter B, $(\tau\beta)_{ij}$ is the effect of the interaction between τ_i and β_j, and ϵ_{ijk} is a random error component. The data arrangement is shown in Table A7.

TABLE A7: Data arrangement for a two-parameter design

		PARAMETER B			
		1	2	...	b
PARAMETER A	1	$Y_{111}, Y_{112}, \ldots, Y_{11n}$	$Y_{121}, Y_{122}, \ldots, Y_{12n}$		$Y_{1b1}, Y_{1b2} \ldots, aY_{1bn}$
	2	$Y_{211}, Y_{212}, \ldots, Y_{21n}$	$Y_{221}, Y_{222}, \ldots, Y_{22n}$		$Y_{2b1}, Y_{2b2}, \ldots, Y_{2bn}$
	⋮				
	a	$Y_{a11}, Y_{a12}, \ldots, Y_{a1n}$	$Y_{a21}, Y_{a22}, \ldots, Y_{a2n}$		$Y_{ab1}, Y_{ab2}, \ldots, Y_{abn}$

Analysis of variance for the data in this format by Statgraphics statistical computer package is generated in an analysis table of the form shown in Table A8.

TABLE A8: Analysis of variance table for two-parameter factorial fpr 1st degree polynomial

Source of variation	Sum of squares	Degrees of freedom	Mean square	F_o	Probability
A treatment	SS_A	a - 1	$MS_A = \frac{SS_A}{(a-1)}$	$F_o = \frac{MS_A}{MS_E}$	P_A
B treatment	SS_B	b - 1	$MS_B = \frac{SS_B}{(b-1)}$	$F_o = \frac{MS_B}{MS_E}$	P_B
Interaction	SS_{AB}	(a-1)(b-1)	$MS_{AB} = \frac{SS_{AB}}{(a-1)(b-1)}$	$F_o = \frac{MS_{AB}}{MS_E}$	P_{AB}

R - squared = R^2 : Sum or errors = SS_E : Mean absolute error = MS_E.

where $MS_E = \frac{SS_E}{(ab(n-1))}$,

R^2 = correlation coefficient and P_A, P_B and P_{AB} are the probabilities that the parameters *can have an F ratio as calculated.* This probability is usually set at 5% as whether to accept or reject the effect as being real or part of the experimental error. The coefficients for equation A5 are *calculated by least squares* regression. The basic principles of two-parameter analysis can be extended to any number as long as the principles of factorial designs are maintained.

A.9 *Normality Assumption and Central Limit Theorem*

The analysis of variance in the previous section is purely an algebraic relationship. However, the use of the F test to determine *whether there are significant differences* in treatment means requires certain assumptions to be satisfied. These assumptions are that the observations are adequately described by the appropriate model such as equation A5, and that the errors are normally and independently distributed with mean zero and constant but unknown variance. In practice, these assumptions usually do not hold exactly. It is therefore, necessary to check the validity of the analysis by examining the residuals prior to accepting a given model. This is discussed in the following section.

Should the residuals analysis fail to satisfy the assumptions it is possible to attempt transformation of data to provide a more reasonable data set which more closely fits these assumptions. The transformations possible are discussed at some length in references [64 and 69]. One method of 'improving' the normality of a data set is by making use of the central limit theorem. There are two important ramifications of this theorem.

Firstly, if random samples, size n, are taken from a distribution with mean x and standard deviation σ, then the sampling distribution will be approximately normal with mean x and standard deviation $\sigma/\sqrt{n}$, the approximation improving as n increases. This simply states that a non-normal distribution can generate approximately normal data by the use of a suitable sampling technique.

The second important ramification is that in the real world of experimentation a measured quantity is usually affected by a series of small errors due to sample and measurement limitations. These can be represented by a linear equation

$$\epsilon = a_1\epsilon_1 + a_2\epsilon_2 + \ldots \quad a_n\epsilon_n \qquad \text{A6}$$

Such a linear function of errors will tend to normality as the number of components becomes large, almost irrespective of the individual distributions of the components. An important proviso is that several of the sources of error must make important contributions to the overall error and that no single error dominates the others.

A.10 *Residuals Analysis*

Residuals analysis is a check after analysis of variance, that there is a good approximation to normality. It is essential to conduct this analysis as maverik points or serious deviations from *normality can result in totally incorrect* conclusions which can lead to costly time wasting. The first step in residuals analysis is a normal probability plot an example of which is shown in Fig. A.13. *This data is drawn from a MOR example. The residuals* should fall close to a straight line. This is approximately true in this case.

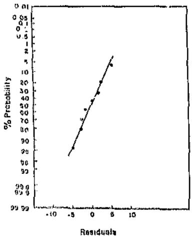

FIGURE A.13: Normal probability plot of residuals

Two other plots of residuals are typically carried out as illustrated in Fig. A.14a and b. The residuals are plotted in the order they are presented and against their predicted values. Any

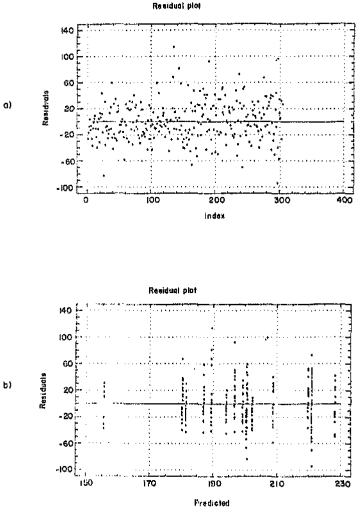

FIGURE A.14: Plot of residuals versus index and predicted values pattern such as a tendency to drift across the zero line or taper off at one end are violations of the assumption of normality and equivalence of variance.

An example of the usefulness of residuals analysis is illustrated in Fig. A.15. In this case one residual is clearly well clear of the normality plot and is therefore regarded as a maverick observation, This is usually due to experimental error and retesting the point can correct the problem.

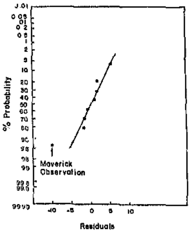

FIGURE A.15: Normal probability plot of residuals showing presence of Maverick observations

APPENDIX B

RESULTS OF FIRST ORDER FACTORIAL

B 1 *Table of Means for Hardness for Each Run*

Level	Count	Average ($\times 10^9$)
1	3	2,87
2	3	2,60
3	3	2,83
4	3	2,86
5	3	5,39
6	3	6,96
7	3	6,14
8	3	7,52
9	3	3,34
10	3	4,05
11	3	3,11
12	3	3,56
13	3	6,52
14	3	6,92
15	3	6,86
16	3	8,21
17	3	8,85
18	3	8,86

B.2 *Analysis of Variance of Hardness Effects*

TABLE B.1: Analysis of variance for hardness

Source of variation		*Sum of* squares	*d.f.*	*Mean* square	*F-ratio*	Sig. level
MAIN EFFECTS		1.74×10^{20}	4	4.34×10^{19}	314.7	.00
DOPANTS		5.96×10^{18}	1	5.96×10^{18}	43.2	.00
TEMP2		1.61×10^{20}	1	1.61×10^{20}	1000.0	.00
STOICH2		1.11×10^{18}	1	1.11×10^{18}	8.1	.07
MILL2		5.40×10^{18}	1	5.40×10^{18}	39.1	.00
2-FACTOR INTERACTIONS		5.17×10^{18}	6	4.34×10^{19}	1000.0	.00
DOPANT2	TEMP2	2.77×10^{18}	1	2.77×10^{18}	20.9	.00
DOPANT2	STOICH2	1.13×10^{17}	1	1.13×10^{17}	.8	.38
TEMP2	STOICH2	2.18×10^{18}	1	2.18×10^{18}	15.8	.00
DOPANT2	MILL2	7.17×10^{15}	1	7.17×10^{15}	.1	.82
TEMP2	MILL2	3.36×10^{16}	1	3.36×10^{16}	.2	.62
STOICH2	MILL2	6.26×10^{16}	1	6.26×10^{16}	.5	.51
RESIDUAL		5.10×10^{18}	37	1.39×10^{17}		

B.3 *Residuals Analysis of Hardness Data*

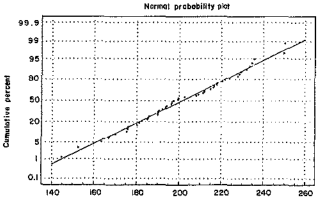

FIGURE B.1: Normal probability plot of residuals for hardness data

APPENDIX C

RESULTS OF SECOND ORDER STRATEGY

C.1 *Regression Analysis for Hardness*

TABLE C.1:

Independent variable	Coefficient $(x10^{10})$	Std. error $(x10^{7})$	t-value	Sig. level
Constant	113,0	9,2	123,0	0,0000
Dopant (A)	-2,5	4,3	-5,7	0,0000
Temperature (B)	1,2	4,3	2,9	0,0054
Time (C)	1,2	4,3	2,8	0,0056
A^2	-2,8	4,7	-5,8	0,0000
B^2	-2,7	4,7	-5,6	0,0000
C^2	-7,3	4,7	-15,4	0,0000
AB	1,1	5,6	2,0	0,0505
AC	0,8	5,6	1,4	0,1664
BC	-1,0	5,6	-1,7	0,0824
ABC	0,6	5,6	-1,1	0,2575

$R^2 = 0,744$

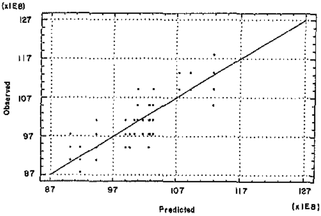

FIGURE C.1: Plot of predicted versus observed data for hardness results

C.2 *Residuals Analysis of Hardness Data*

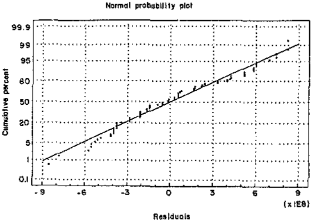

FIGURE C.2: Normal probability plot of residuals

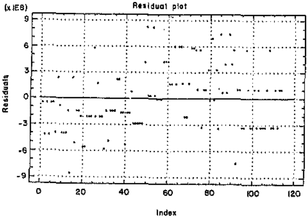

FIGURE C.3: Plot of hardness residuals in order of measurement

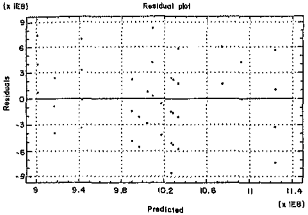

FIGURE C.4: Plot of hardness residuals against predicted level

C.3 *Average Results for Hardness*

TABLE C.2: Average results for hardness

Level	Count	Average (x10^9)	Level	Count	Average (x10^9)
1	6	10,2	10	6	10,9
2	6	9,2	11	6	10,7
3	6	10,2	12	6	10,3
4	6	10,0	13	6	11,3
5	6	10,3	14	6	9,4
6	6	9,9	15	6	9,0
7	6	10,3	16	6	11,3
8	6	10,0	17	6	11,3
9	6	10,1			

C.4 *Regresson Results for Strength*

TABLE C.3: Regression results for strength

Independent variable	Coefficient ($x10^{10}$)	Std. error ($x10^{7}$)	t-value	Sig. level
Constant	227,6	4,7	48,8	0,0000
Dopant (A)	1,5	2,2	0,7	0,4786
Temperature (B)	3,3	2,2	1,5	0,1393
Time (C)	-5,7	2,2	-2,6	0,0125
A^2	-10,4	2,4	-4,3	0,0001
B^2	-0,5	2,4	-0,2	0,8439
C^2	-21,6	2,4	-9,0	0,0000
AB	2,2	2,9	0,8	0,4428
AC	1,3	2,9	0,5	0,6399
BC	2,1	2,9	0,7	0,4603
ABC	-0,7	2,9	-0,3	0,7976

$R^2 = 0,65$ Standard error = 14 Mean average error = 10,4

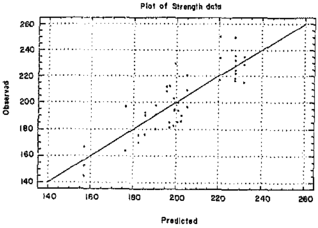

FIGURE C.5: Plot of regression estimates vs observed data for strength

C.5 *Residuals Analysis for Strength Data*

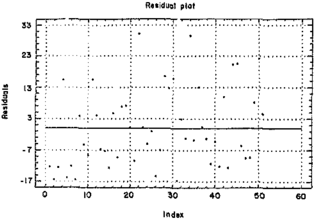

FIGURE C.6: Plot of strength residuals in order of testing

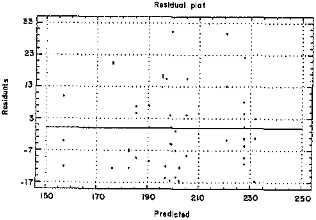

FIGURE C.7: Plot of strength residuals against estimated values

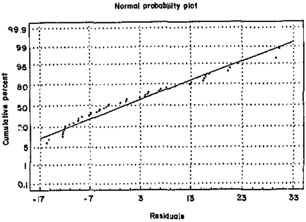

FIGURE C.8: Normal probability plot of strength data

Author Carr N S
Name of thesis Optimization Of Properties Of Zirconia-mullite Ceramics. 1989